https://ntrs.nasa.gov/search.jsp?R=19700022542 2020-03-12T02:17:07+00:00Z

TECH LIBRARY KAFB, NM
0060869

NASA CONTRACTOR REPORT

NASA CR-1
c.1

LOAN COPY: RETURN TO
AFWL (WLOL)
KIRTLAND AFB, N MEX

NASA CR-1548

STAGNATION POINT ANALYSIS OF COUPLED VISCOUS-RADIATING FLOW WITH MASSIVE BLOWING

by K. H. Wilson

Prepared by
LOCKHEED AIRCRAFT CORPORATION
Palo Alto, Calif.
for Ames Research Center

RECEIVED
29 JUN 70
Technical Library
AFWL (WLOL)
Kirtland AFB, N. Mex.

NATIONAL AERONAUTICS AND SPACE ADMINISTRATION • WASHINGTON, D. C. • JUNE 1970

call no.
NASA CR-1548
TECH LIBRARY KAFB, NM
0060869

STAGNATION POINT ANALYSIS OF COUPLED VISCOUS-RADIATING FLOW WITH MASSIVE BLOWING

By K. H. Wilson

Jun 70

note: 1 of 2 vols. under contract NAS-7-632.
Forward,

Prepared under Contract No. NAS 7-632 by
LOCKHEED AIRCRAFT CORPORATION
Palo Alto, Calif.

for Ames Research Center

NATIONAL AERONAUTICS AND SPACE ADMINISTRATION

For sale by the Clearinghouse for Federal Scientific and Technical Information
Springfield, Virginia 22151 – CFSTI price $3.00

ABSTRACT

An analysis of the fully coupled viscous, radiating flow at the stagnation point of an ablating blunt body at hyperbolic entry conditions is presented. An exact numerical solution to the momentum equation has been developed which replaces the integral method approach employed in previous studies. This improved analysis yields an accurate solution to the conservation equations under conditions of massive blowing where the viscous transport layer is detached from the surface. The radiative transport model has been modified to obtain an accurate calculation of both continuum and line transport for arbitrary mixtures of H, C, N and O atoms. A comparison of our current results for the stagnation point surface radiative flux at hyperbolic velocities with recent results of a number of other investigators show that (for the case of a non-ablating surface), when all important radiating processes are accounted for, agreement to within about 20% exists. For the case of the blunt body heating problem with large surface mass injection (of predominantly hydrogen-carbon ablation gases) the role of atomic line radiative transport in the ablation gases is clarified. It is found that strong re-radiation in line transitions from the heated carbon atoms negates the absorption of nitrogen-oxygen line radiation by the ablation gases resulting in no net decrease in line radiation due to mass injection. When continuum processes only are considered, mass injection rates of 10% of the free stream mass flux decrease the surface flux to roughly 60% of hte non-blowing level. However, when lines are properly accounted for, the surface radiative flux is then reduced to only about 80% of the non-blowing level.

ACKNOWLEDGMENTS

The author emphasizes the fundamental contributions of Professor Ralph Greif, University of California, in the formulation of the radiative transport analysis given herein. The author also expresses his appreciation for the conscientious efforts of Miss H. R. Kirch who developed the computer code and many of the numerical techniques required in obtaining the solutions.

NOMENCLATURE

A	absorption-weighted equivalent width of a line or line group
A^*_{ij}	collision integral ratio used in transport properties
B_ν	Planckian spectral radiant intensity
C_i	elemental mass fraction of i^{th} element
C_j	mass fraction of j^{th} species
C_v	mass fraction of ablation products
C_P	specific heat
$\bar{C}_P$	frozen specific heat
c	velocity of light
D	effective diffusion coefficient
D_k	spectral interval covered by a line group
E_ν	monochromatic continuum emissivity
e	charge on electron, esu
ϵ_n	exponential integral function
F	radiative flux; also normalized stream function
f_w	blowing parameter, $\dot{m}_e(Re_\delta/\rho_w\mu_w)^{1/2}$
f	normalized tangential velocity function u/u_δ
f^*_i	averaged line f-number for element i
$f_{nn'}$	line absorption f-number
g	normalized total enthalpy function H/H_δ
H	total enthalpy
h	static enthalpy; also Planck constant

I_o, I_1	modified Bessel functions
I	radiative intensity
K	radius of curvature of reference coordinate surface
$\tilde{K}$	arc-length in x-direction
$\bar{k}$	frozen thermal conductivity
k	total thermal conductivity; also Boltzman constant
Le_j	Lewis number
ℓ	reciprocal average direction cosine
m	mass of electron
$\dot{m}$	mass flux of ablation products
N	number density
n_i	number of lines in equivalent line group for element i
p	pressure
Pr	Prandtl number
Q	radiative flux divergence
$Q^{L,C}$	energy emitted by line, absorbed by continuum
$Q^{C,L}$	energy emitted by continuum, absorbed by line
$Q^{L,L}$	energy emitted and absorbed by line
R	body radius
Re_δ	Reynolds number $\rho'_\infty U'_\infty R'/\mu'_\delta$
r	distance of point x, y from axis of symmetry
S	integrated line absorption
Sc_δ	Schmidt number $\mu'_\delta/\rho'_\delta D'_\delta$
T	temperature
U_∞	free-stream velocity

u	velocity component parallel to body
v	velocity component normal to surface
W	flux equivalent width of a line or group of lines
x_j	mole fraction of species j
x,y	body-oriented coordinate system
z	variable in line transport analysis
α	line overlap variable
$(\alpha_v)_i$	number of grams of element i per gram of pyrolysis products
$(\alpha_a)_i$	number of grams of element i per gram of air
γ_i^*	averaged line half-width for element i
$\bar{\gamma}$	spatially averaged half-width
δ	physical shock detachment distance
$\tilde{\delta}$	transformed shock detachment distance
η	transformed y coordinate
ϵ	density ratio across shock $\rho'_\infty/\rho'_\delta$
ρ	density
λ	parameter in momentum equation, $\rho_w\mu_w/\epsilon^2 Re_\delta$
μ	viscosity; also volumetric absorption coefficient
Γ	line transport function
Λ	line transport function
ξ	transformed x-coordinate
τ_ν	optical depth at frequency ν
ψ	stream function
ω	solid angle; also chemical species source term
ϕ	angle between shock normal and symmetry axis, also error integral
ϕ_{ij}	function defined in transport property determination

σ	absorption cross section

Subscripts

i	i^{th} element
j	j^{th} species
k	equivalent line number
m	denotes m^{th} line in a line group
w	body surface quantities
δ	quantities immediately behind shock
∞	free-stream condition
o	line center frequency

Superscripts

C	continuum contribution
L	line contribution
'	denote dimensional variable

CONTENTS

FOREWORD

This report is one of two volumes covering work performed for the National Aeronautics and Space Administration Headquarters, Office of Advanced Research and Technology, under the terms and specifications of Contract NAS 7-632, issued through NASA Resident Office, Jet Propulsion Laboratory, 4800 Oak Grove Drive, Pasadena, California. Technical Monitor of this contract was Mr. William Page, Hypersonic Free-Flight Branch, NASA Ames Research Center, Moffett Field, California.

The work was performed in the Aerospace Sciences Laboratory (R. Capiaux, Manager), of the Lockheed Palo Alto Research Laboratory.

Section 1
INTRODUCTION

The problem of the determination of the stagnation point heating to a body entering the Earth's atmosphere at velocities exceeding escape speed (i.e. hyperbolic entry) has received considerable attention in recent years. The earliest works, e.g. Howe (Ref. 1) and Wilson and Hoshizaki (Refs. 2, 3) used a grey-gas radiative transport model which was tantamount to an optically thin analysis. The calculated heating levels thus predicted were unrealiable. The first realistic treatment of the spectral character of air emission and hence the proper accounting of self-absorption and radiative cooling appears to be that of Hoshizaki and Wilson (Ref. 4). This work considered only the continuous radiative transitions in high temperature air. However, the work of Biberman and his colleagues (Ref. 5) convincingly demonstrated that, at the thermodynamic conditions and pathlengths anticipated for hyperbolic entry, atomic line transitions would be equal in importance to the continuous transitions. Subsequently, a number of investigators, using various line transport models, presented results for combined continuum and line processes. The inclusion of line transport was reported by Rigdon et al. (Ref. 6), Page et al. (Ref. 7), Chin (Ref. 8) and the unpublished work of Wilson and Hoshizaki (Ref. 9). Some major discrepancies in the surface radiative flux existed due to differences in the basic absorption coefficient data as well as the transport models.

Another area of significant uncertainty was the effect of ablation product gases injected into the shock layer on the radiative heating. This question was initially examined by Hoshizaki and Wilson (Ref. 4) but their treatment of the absorption coefficient for the ablation gases was much too crude. An improved calculation was reported by Hoshizaki and Lasher (Ref. 10) which incorporated the recent results of Wilson and Hoshizaki (Ref. 9). The calculation of Ref. 10 considered only continuum emission. Recently Chin (Ref. 8) reported the results of an investigation of mass injection effects including line transitions for nitrogen atoms but not those of the atoms present in the ablation gases.

The work reported herein is a continuation of the study of fully coupled viscous, radiating shock layers including mass injection. The result of this work is two major improvements over the analysis presented in Ref. 9. Firstly, the previous integral-method solution has been discarded in favor of a full calculation of the differential momentum equations. The computational method developed to obtain solutions to the differential momentum equations is fast and numerically stable. Moreover a technique was devised to obtain solutions to all the governing conservation equations under conditions of arbitrarily large mass injection (Provided, of course, the fundamental condition of a thin shock layer is not violated). Secondly, the line transport model was revised to provide a consistent treatment to the nonhomogeneous line transport problem and to provide an accurate calculation of transport in mixtures of hydrogen, carbon, nitrogen, and oxygen atoms. As a result of these improvements we have considerably increased the accuracy of the computational code.

Finally, the proper accounting of line transport in mixtures of atomic species shows that (for the flight condition examined) large rates of injection of hydrogen-carbon ablation gases are ineffective in reducing the line contribution to the radiative flux.

Section 2

MATHEMATICAL DEVELOPMENT

2.1 GOVERNING EQUATIONS

Our point of departure is the Navier-Stokes equations simplified under the thin shock layer approximation as developed by Ho and Probstein (Ref. 11).* The governing equations are expressed in terms of the body-oriented coordinate system shown in the sketch below.

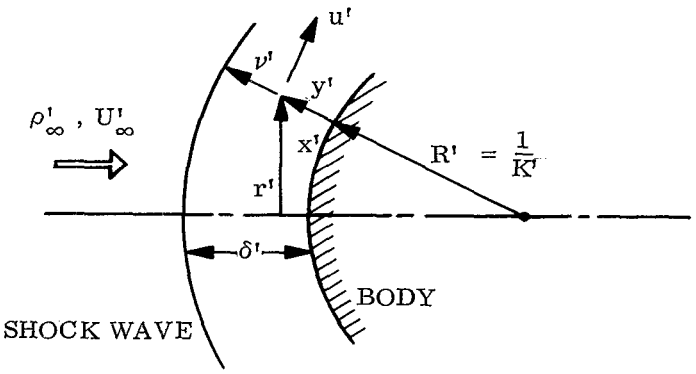

COORDINATE GEOMETRY

Here x' is the distance measured parallel to the body (from the stagnation point), y' is the distance measured normal to the body, and K' is the local body curvature. The distance of the point x', y' from the symmetry

---

* It should be pointed out that these equations are simpler in form than those used previously in our viscous radiating shock layer investigation (Refs. 4,9,10). These earlier formulations were inconsistent in that they contained terms of order $1/\epsilon\ Re\delta$. Although inclusion of these unnecessary higher order terms did not effect the numerical solutions previously obtained, we will use the above consistent set of equations as they afford a cleaner formulation.

axis is related to x' through the metric variable $\tilde{K}$ by

$$dr' = \tilde{K}(x')\, dx'$$

where

$$\tilde{K} = 1 + K'y' \tag{1}$$

Then the conservation equations, valid to order $(\epsilon^2 Re_\delta)^{-1}$, are

mass:
$$\frac{\partial}{\partial x'}(r'\rho'u') + \frac{\partial}{\partial y'}(r'\tilde{K}\rho'v') = 0 \tag{2}$$

x-momentum:
$$\rho'u'\frac{\partial u'}{\partial x'} + \tilde{K}\rho'v'\frac{\partial u'}{\partial y'} + K'\rho'u'v' = -\frac{\partial p'}{\partial x'} + \frac{\partial}{\partial y'}\left(\mu'\frac{\partial u'}{\partial y'}\right) \tag{3}$$

y-momentum:
$$\rho'u'\frac{\partial v'}{\partial x'} + \tilde{K}\rho'v'\frac{\partial v'}{\partial y'} - K'\rho'u'^2 = -\frac{\partial p'}{\partial y'} \tag{4}$$

energy:
$$\rho'u'\frac{\partial H'}{\partial x'} + \tilde{K}\rho'v'\frac{\partial H'}{\partial y'} = \frac{\partial}{\partial y'}\left[\frac{\mu'}{Pr}\frac{\partial H'}{\partial y'} + \rho'\sum_j D'h_j'\frac{\partial C_j}{\partial y'}\right] + \frac{\partial}{\partial y'}\left[\frac{\mu'}{2}\left(1 - \frac{1}{Pr}\right)\frac{\partial u'^2}{\partial y'}\right] + Q' \tag{5}$$

species:
$$\rho'u'\frac{\partial C_j}{\partial x'} + \tilde{K}\rho'v'\frac{\partial C_j}{\partial y'} = \frac{\partial}{\partial y'}\left(\rho'D'\frac{\partial C_j}{\partial y'}\right) + \omega_j' \tag{6}$$

In the energy equation, the symbol Q' is defined as the radiative flux divergence, the precise form for which is taken up in Section 3.

Note that in the energy and species conservation equations, the species mass

flux is given by the binary approximation (Fick's law), $\rho' D' \frac{\partial C_j}{\partial y'}$ where a single, species independent diffusion coefficient applies. This model of the true multicomponent diffusion process was proposed by Lees, (Ref. 12). The validity of this model will not be pursued in detail other than to recognize that it is valid when the gas mixture consists of two groups of species. The molecular weight of the members of each group are roughly the same but the mean molecular weight of the two groups may vary widely. The application of this model to problems involving mass injection of hydrogen is clearly a crude approximation as it is physically clear that hydrogen will diffuse further into the shock layer than relatively heavy species composed of carbon, nitrogen and oxygen. Some simplified, uncoupled studies have shown that even large differences in the hydrogen concentration distribution show little effect on the primary quantity of interest, viz., the radiative energy transport to the body surface. Finally, we note that Kendall and Bartlett (Ref.13) have proposed a model which offers a good approximation to a multicomponent mixture of varying molecular weight and which is, computationally, relatively simple. Unfortunately, time limitations prevented the incorporation of their model into this analysis. However, for reference purposes, the formulation of their model to the viscous shock layer problem is described in Appendix C.

Finally, we note that the above set of conservation laws must be augmented by appropriate equations of state. In the numerical method to follow, these equations of state are obtained through a detailed thermochemical calculation which automatically handles the varying elemental composition conditions which exist when mass injection is considered. A description of the thermochemical calculation is given in Section 4.

It is convenient to nondimensionalize and normalize all quantities to O(1) as follows:

$$u = \frac{u'}{U'_\infty} \quad ; \quad v = \frac{v'}{\epsilon U'_\infty} \quad ; \quad x = \frac{x'}{R'} \quad ; \quad y = \frac{y'}{\epsilon R'} \quad ; \quad r = K'r'$$

$$\rho = \frac{\rho'}{\rho'_\delta} \quad ; \quad K = R'K' \quad ; \quad \mu = \frac{\mu'}{\mu'_\delta} \quad ; \quad p = \frac{p'}{\rho'_\infty U'^2_\infty}$$

$$H = \frac{H'}{\frac{1}{2} U'^2_\infty} \quad ; \quad Q = \frac{R'Q'}{\epsilon \rho'_\infty U'^3_\infty} \quad ; \quad \omega_j = \frac{\omega'_j R'}{\rho'_\infty U'_\infty}$$

Then the conservation equations become

mass:
$$\frac{\partial}{\partial x} (r\rho u) + \frac{\partial}{\partial y} (r\tilde{K}\rho v) = 0 \tag{7}$$

x-momentum:
$$\rho u \frac{\partial u}{\partial x} + \tilde{K}\rho v \frac{\partial u}{\partial y} + K\rho uv = - \epsilon \frac{\partial p}{\partial x} + \frac{1}{\epsilon^2 Re_\delta} \frac{\partial}{\partial y} (\mu \frac{\partial u}{\partial y}) \tag{8}$$

y-momentum:
$$\epsilon\rho u \frac{\partial v}{\partial x} + \epsilon K\rho v \frac{\partial v}{\partial y} - K\rho u^2 = - \frac{\partial p}{\partial y} \tag{9}$$

energy:
$$\rho u \frac{\partial H}{\partial x} + \tilde{K}\rho v \frac{\partial H}{\partial y} = \frac{1}{\epsilon^2 Re_\delta} \frac{\partial}{\partial y} \left[\frac{\mu}{Pr} \frac{\partial H}{\partial y} + \frac{1}{Sc_\delta} \Sigma \rho D h_j \frac{\partial C_j}{\partial y} \right] + \frac{1}{\epsilon^2 Re_\delta} \frac{\partial}{\partial y} \left[\mu \left(1 - \frac{1}{Pr}\right) \frac{\partial u^2}{\partial y} \right] + \epsilon Q \tag{10}$$

species:
$$\rho u \frac{\partial C_j}{\partial x} + \tilde{K}\rho v \frac{\partial C_j}{\partial y} = \frac{1}{\epsilon^2 Re_\delta Sc_\delta} \frac{\partial}{\partial y} (\rho D \frac{\partial C_j}{\partial y}) + \omega_j \tag{11}$$

2.2 SOLUTION TO THE MOMENTUM EQUATIONS

The momentum equations are now recast in a form convenient for numerical calculation. First the transformed coordinate η, ξ are defined,

$$\eta = \frac{\int_o^y \rho \frac{r}{r_w} dy}{\int_o^\delta \rho \frac{r}{r_w} dy} = \frac{\int_o^y \rho \frac{r}{r_w} dy}{\tilde{\delta}} \tag{12a}$$

$$\xi = x \tag{12b}$$

Now introduce a nondimensional stream function ψ defined by

$$r\rho u = \frac{\partial \psi}{\partial y})_x \tag{13a}$$

$$\tilde{K} r \rho v = - \frac{\partial \psi}{\partial x})_y \tag{13b}$$

and the normalized stream function

$$F = - \frac{\psi}{\rho_\delta u_\delta r_w} \tag{14}$$

We obtain from the transformation equations the relation

$$f \equiv \frac{u}{u_\delta} = \frac{1}{\tilde{\delta}} \frac{\partial F}{\partial \eta})_\xi \tag{15}$$

Using Eqs. (12)-(15), the x-momentum and y-momentum equations are combined.

After algebraic manipulation and retaining only terms of $O(\epsilon)$* and, further, now restricting the analysis to the stagnation region where

$$\left.\frac{\partial f}{\partial \xi}\right|_{\eta} = 0 \tag{17}$$

the following form of the combined momentum equations is obtained,

$$\frac{\lambda}{\tilde{\delta}^2}\frac{d^2 f}{d\eta^2} + 2\frac{F}{\tilde{\delta}}\frac{df}{d\eta} - f^2 + \frac{3\epsilon}{\rho} = 0 \tag{18}$$

where $\lambda = \rho_w \mu_w / \epsilon^2 Re_\delta$. In arriving at Eq. (18) we have made two additional simplifying approximations. These are

$$\left(\frac{r}{r_w}\right) \sim 1$$

$$\rho\mu \sim \text{constant} = \rho_w \mu_w$$

The first of these, $(r/r_w) \sim 1$, is quite reasonable for the thin shock layers of interest (typically $\epsilon = .06$ and note that $1 \leq r/r_w \lesssim 1 + \epsilon$). The second approximation is potentially more serious since $\rho\mu$ varies considerably through the shock layer. However, as will be demonstrated by the numerical comparison shown in Section 5, this approximation does not introduce significant error in the shock layer velocity distribution solution. Moreover, by using this approximation, the resulting simplified momentum equation can be solved in a relatively simple manner for the difficult case of viscous flow with large

*Essentially we replace the full y-momentum equation by

$$\frac{\partial p}{\partial y} = K\rho u^2$$

in evaluating the pressure gradient term in the x-momentum equation.

mass injection.

Equation (18), together with the auxiliary equation for the stream function

$$\frac{dF}{d\eta} = \tilde{\delta}\, f \tag{19}$$

are the system of simultaneous nonlinear differential equations determining the velocity field. The boundary conditions are

$$\text{at } \eta = 0 \qquad f = 0 \tag{20a}$$

$$F = -\dot{m}/2 \tag{20b}$$

$$\text{at } \eta = 1 \qquad f = 1 \tag{20c}$$

The principal nonlinear term f^2 in Eq. (18) can be eliminated by differentiating Eq. (18) and using Eq. (19).* The resulting equation is

$$\frac{d^3f}{d\eta^3} = -3\epsilon\left(\frac{\tilde{\delta}}{\sqrt{\lambda}}\right)^2 \frac{d\,1/\rho}{d\eta} - \frac{2\tilde{\delta}F}{\sqrt{\lambda}}\frac{d^2f}{d\eta^2} \tag{21}$$

with the boundary conditions,

$$f = 0 \tag{22a}$$

$$\eta = 0$$

$$\frac{d^2f}{d\eta^2} = -\frac{2\tilde{\delta}F}{\sqrt{\lambda}}\frac{df}{d\eta} - 3\epsilon\left(\frac{\tilde{\delta}}{\sqrt{\lambda}}\right)^2 \frac{1}{\rho} \tag{22b}$$

*The author is indebted to Dr. Y. S. Chou of the Lockheed Palo Alto Research Laboratory for the above solution to the momentum equation.

$$\eta = 1 \qquad f = 1 \tag{22c}$$

The solution to Eq. (21) proceeds as follows. The pressure across the shock layer (to order ϵ) at the stagnation point is constant at the shock value,

$$p = p_s = (1 - \epsilon) \tag{23}$$

Assuming the enthalpy distribution is known (as a result of an iterative solution to the energy equation), the density distribution is obtained from the state relations. Then if an estimate to the velocity field $f^i(\eta)$ is made, the stream function can be determined from the integration of Eq. (19) with $\tilde{\delta}$ given by

$$\tilde{\delta} = \frac{(1 + \dot{m})}{2 \int_0^1 f(\eta) d\eta} \tag{24}$$

With $F(\eta)$ now known, Eq. (21) is a linear equation (in $\frac{d^2 f}{d\eta^2}$) from which a new solution $f^{i+1}(\eta)$ can be obtained directly. The sequence of calculations is repeated until a satisfactorily converged solution (normally within 1%) is obtained.

For small values of mass injection, more precisely when the parameter $\dot{m}/\sqrt{\lambda} \lesssim 1$, the solution to Eq. (21) is straightforward. However, as $\dot{m}/\sqrt{\lambda}$ becomes much greater than unity, numerical difficulties are encountered. The difficulties originate from trying to maintain numerical precision when taking the difference of exponentially large numbers. These numerical difficulties reflect the physical fact that for $\dot{m}/\sqrt{\lambda} > 1$, the flow near the surface is an inviscid inner layer whose velocity gradient $df/d\eta$ at the surface is given by the pressure gradient term $3\epsilon/\rho$. The inner layer is

physically decoupled from the boundary condition behind the shock. Hence the attempt to solve the entire shock layer as a viscous flow with boundary conditions given at the body surface and shock leads to numerical difficulties.

We have circumvented the numerical problems by taking advantage of the fact that a portion of the shock layer near the surface is characterized as an inviscid flow. Let η^* be the extent of this inviscid region. Then we drop the viscous term in Eq. (18) and solve for $f(\eta)$ from

$$0 \le \eta \le \eta^*$$

$$\frac{df}{d\eta} = \frac{\tilde{\delta}[f^2(\eta) - 3\epsilon/\rho]}{2F(\eta)} \tag{25}$$

with the boundary condition

$$\eta = 0 \qquad f = 0 \tag{26}$$

and, again $F(\eta)$ is known. In the outer region we again solve Eq. (21) as before, except that the boundary conditions now become,

$$\eta = \eta^* \qquad f = f(\eta^*) \tag{27a}$$

$$\frac{d^2f}{d\eta^2} = 0 \tag{27b}$$

$$\eta = 1 \qquad f = 1 \tag{27c}$$

The problem with this method, of course, is to determine η^* which is defined by the criterion that for $\eta \le \eta^*$ the flow is inviscid. Unfortunately there

is no exact (analytical or numerical) method for selecting η^* since the flow becomes inviscid only in an asymptotic sense. Note that η^* must be such that the argument of the exponential term which appears in the solution to Eq. (21) is less than about 10.* That is, η^* must be chosen so that

$$P(\eta) = -\frac{2\tilde{\delta}}{\sqrt{\lambda}} \int_{\eta^*}^{\eta} F(\eta')\, d\eta' \lesssim 10$$

In practice we have used the simple criterion that η^* is the first value of η such that

$$F(\eta) \geq \left(-\frac{\dot{m}}{2}\right) * \text{MAX} \qquad (\text{MAX a parameter})$$

where, of course, $(-\dot{m}/2)$ is the value of $F(\eta = 0)$. The stream function distribution $F(\eta)$ for two values of the mass injection parameter $\dot{m}/\sqrt{\lambda}$ is shown in Fig. 1. Note that for the small mass injection parameter case, the stream function increases much more rapidly than for the large mass injection parameter problem. Hence this simple criterion appropriately scales the extent of the inner inviscid region with the mass injection level. The validity of assuming an inner inviscid region of various extent can only be ascertained by comparison with an exact solution. In Fig. 2 an exact solution is given to the full viscous problem for the case of $\dot{m}/\sqrt{\lambda} = 2.04$ as obtained by double-precision calculation. Also shown in Fig. 2 are the results of using an inner inviscid solution of varying extent. It can be seen that selecting MAX = .75 yields accurate results

*The value of 10 is associated with the fact that $e^{10} \sim 0\ (10^4)$. Hence when differences of numbers of this size are taken with normal machine precision (7 usable significant figures) this gives values accurate to 3 significant figures.

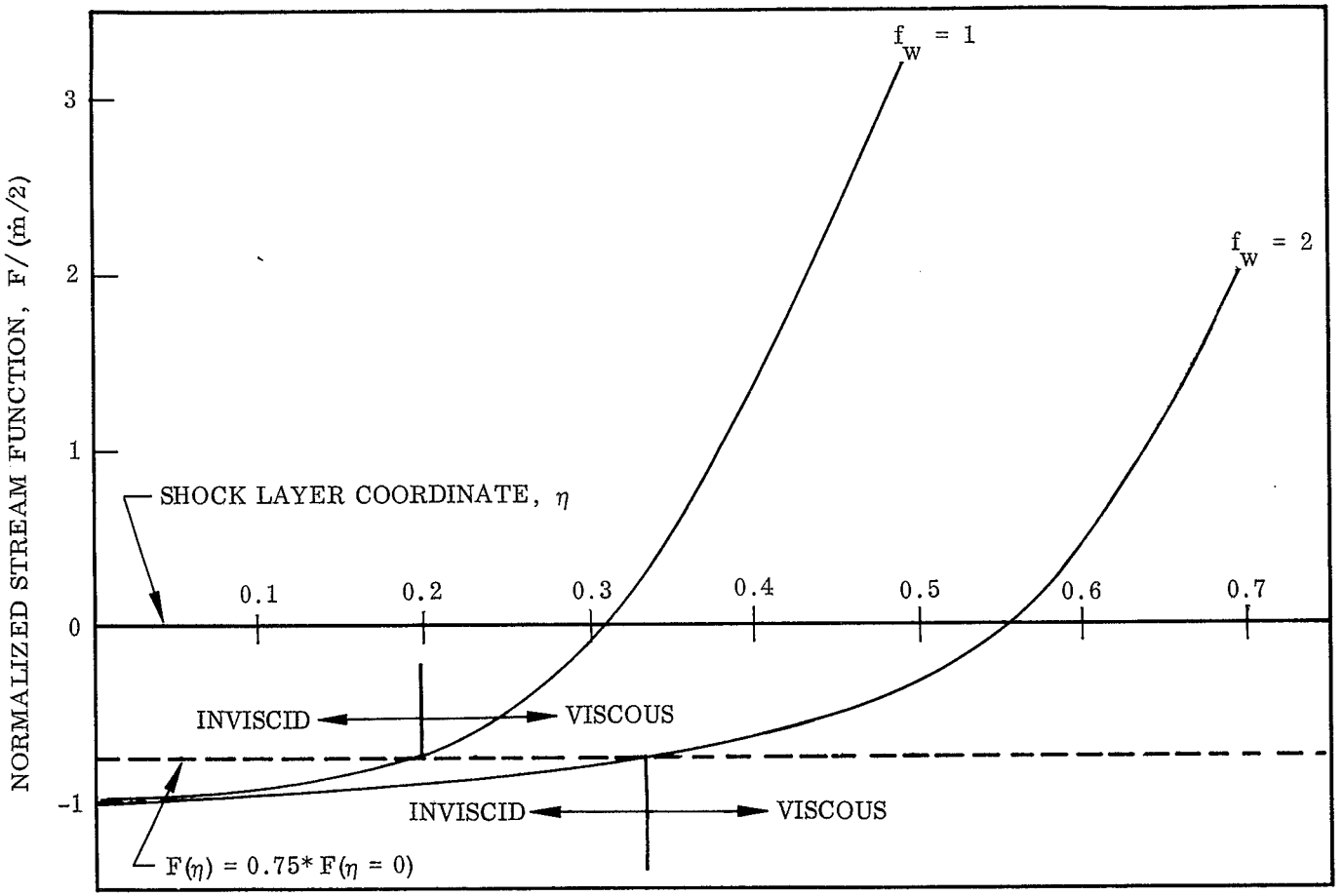

Fig. 1 Stream Function Distribution for Two Mass Injection Cases

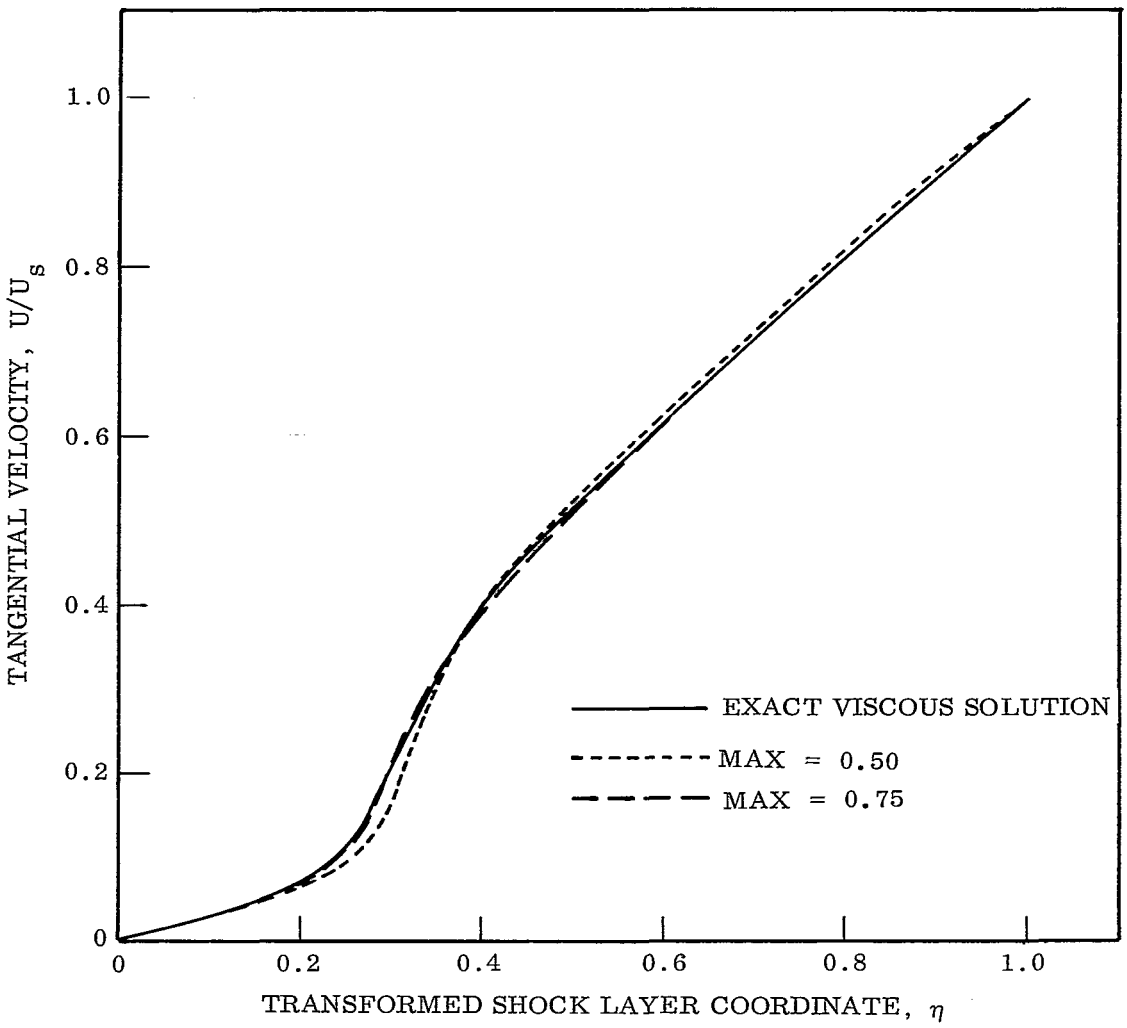

Fig. 2 Comparison of Exact and Approximate Tangential Velocity Solutions

for the approximate inviscid-viscous flow solution. This value of MAX = .75 was used in the numerical solutions presented in Section 5 whenever $\dot{m}/\sqrt{\lambda} > 1$. For $\dot{m}/\sqrt{\lambda} \leq 1$, the full viscous calculation was used.

2.3 SOLUTION TO THE SPECIES DIFFUSION EQUATION

Under the binary diffusion model used to write the species conservation equation in the form given by Eq. (11), it is not necessary to calculate the transport of each species directly. Rather we adopt the concept outlined by Lees (Ref. 12) in which the species equation is summed over all species containing a given element i (details are available in Ref. 14). When this is done we obtain the following equation expressing conservation of each element, i.

$$\rho u \frac{\partial C_i}{\partial x} + \tilde{K} \rho v \frac{\partial C_i}{\partial y} = \frac{1}{\epsilon^2 Re_\delta Sc_\delta} \frac{\partial}{\partial y} \left(\rho D \frac{\partial C_i}{\partial y} \right) \tag{28}$$

Moreover, since a single diffusion coefficient exists, it is clear that all the elemental components of the injected gas will diffuse at the same rate. Hence the diffusion is actually a binary process of "ablation gases" diffusing into air. We denote by C_v the mass fraction of these ablation gases. Then the mass fraction of elemental i is

$$C_i = (\alpha_v)_i \, C_v + (\alpha_a)_i \, [1 - C_v] \tag{29}$$

where $(\alpha_v)_i$ = mass fraction of element i in ablation products

$(\alpha_a)_i$ = mass fraction of element i in air

Equation (28) is now expressed in terms of the diffusion of ablation product gases,

$$\rho u \frac{\partial C_v}{\partial x} + \tilde{K}\rho v \frac{\partial C_v}{\partial y} = \frac{1}{\epsilon^2 Re_\delta Sc_\delta} \frac{\partial}{\partial y} \left(\rho D \frac{\partial C_v}{\partial y}\right) \tag{30}$$

The boundary condition at the body surface follows from an assumed steady state mass balance across an interface region across which the decomposition of the surface occurs instantaneously. The boundary condition at the shock derives from the condition that for a viscous layer analysis there can be no significant gradients due to transport effects right behind the shock. Then at the shock the ablation gas concentration must vanish. If we now transform Eq. (30) to η, ξ coordinates and restrict the analysis to the stagnation region, we obtain

$$\frac{d}{d\eta} \left(\rho^2 D \frac{dC_v}{d\eta}\right) + \left(\epsilon^2 \tilde{\delta} Re_\delta Sc_\delta\right) 2F \frac{dC_v}{d\eta} = 0 \tag{31}$$

with the boundary conditions

$$\eta = 0 \qquad \rho^2 D \frac{dC_v}{d\eta} = - \epsilon^2 Re_\delta Sc_\delta \dot{m}\tilde{\delta}(1 - C_v) \tag{32a}$$

$$\eta = 1 \qquad C_v = 0 \tag{32b}$$

Consistent with the treatment of the momentum equations for the large mass injection limit, the ablation gas conservation equation is solved separately for an inner inviscid region and patched to an outer viscous solution. Then we have for the inner inviscid region,

$$0 \le \eta \le \eta^* \qquad C_v \equiv 1 \tag{33}$$

and for the outer region we solve Eq. (31) subject to the boundary conditions,

$$\eta = \eta^* \qquad \rho^2 D \frac{dC_v}{d\eta} = - \epsilon^2 Re_\delta Sc_\delta \; 2F(\eta^*)[1 - C_v(\eta^*)] \tag{34a}$$

$$\eta = 1 \qquad C_v = 0 \tag{34b}$$

Note that the boundary condition, Eq. (34a), does not identically match $C_v(\eta^*)\big|_{outer} = C_v(\eta^*)\big|_{inner} = 1$. However, for all practical purposes, under the large mass injection conditions ($\dot{m}/\sqrt{\lambda} > 1$) where the inner inviscid layer is used, the solution to Eq. (31) in the viscous layer yields $C_v(\eta^*)\big|_{outer} = 1$.

2.4 SOLUTION TO THE ENERGY EQUATION

Before recasting the energy equation for numerical solution it is essential to express the diffusional enthalpy transport term as

$$\frac{\partial C_j(T,p,C_i)}{\partial y} = \frac{\partial C_j}{\partial T} \frac{\partial T}{\partial y} + \sum_i \frac{\partial C_j}{\partial C_i} \frac{\partial C_i}{\partial y} \tag{35}$$

Then using Eq. (35) to rewrite Eq. (10) we obtain (further details can be found in Ref. 14),

$$\rho u \frac{\partial H}{\partial x} + \tilde{K} \rho v \frac{\partial H}{\partial y} = \frac{1}{\epsilon^2 Re_\delta} \frac{\partial}{\partial y} \frac{\mu}{Pr} \left[\frac{\partial H}{\partial y} + \sum_i \sum_j (Le-1) \frac{\partial C_j}{\partial C_i} \frac{\partial C_i}{\partial y} \right] + \frac{\partial}{\partial y} \left[\mu \left(1 - \frac{1}{Pr}\right) \frac{\partial u^2}{\partial y} \right] + \epsilon Q \tag{36}$$

The calculation of the concentration derivatives $\partial C_j / \partial C_i$ is very difficult (see Ref. 14). Moreover, we find that $Le \approx 1$ and that a posterori calculations

show the term

$$\frac{\mu}{Pr} \sum_i \sum_j (Le-1) \frac{\partial C_j}{\partial C_i} \frac{\partial C_i}{\partial y}$$

contributes only slightly to the collisional transport. Hence we will be content to make the approximation $Le \equiv 1$, and thus drop this term from the energy equation.

Now transforming Eq. (36) to η, ξ coordinates and restricting the analysis to the stagnation region we obtain,

$$\frac{d}{d\eta} \left(\frac{\rho\mu}{Pr} \frac{dg}{d\eta}\right) + \epsilon^2 Re_\delta \tilde{\delta}\, 2F \frac{dg}{d\eta} + \epsilon^3 Re_\delta \tilde{\delta} \left(\frac{Q}{\rho}\right) \tag{37}$$

where we have introduced $g = H/H_\delta$ and also again used the approximation $(r/r_w) \sim 1$. Following the treatment used in solving the momentum and diffusion equations for the large mass injection case, we introduce an inner inviscid region. Dropping the viscous term in Eq. (37), the enthalpy distribution in the inner inviscid region is calculated from

$$\text{for} \quad 0 \le \eta \le \eta^* \qquad \frac{dg}{d\eta} = \frac{\epsilon\tilde{\delta}Q}{2F\rho} \tag{38}$$

with the boundary condition

$$\eta = 0 \qquad g = g_w \tag{39}$$

For the outer viscous region we calculate $g(\eta)$ from Eq. (37) using the boundary conditions

$$\eta = \eta^* \qquad g = g(\eta^*) \tag{40a}$$

$$\eta = 1 \qquad g = 1 \tag{40b}$$

In solving Eqs. (37) and (38) it has been tacitly assumed that the flux divergence term is known. The procedure is to estimate the enthalpy distribution $g^i(\eta)$ and solve the momentum and diffusion equations. Then along with p = constant, we have completely defined the distribution of thermodynamic variables through the shock layer in physical coordinates. The flux divergence may then be calculated by the methods outlined in the next section. This allows a new enthalpy distribution $g^{i+1}(\eta)$ to be calculated. The entire process is repeated until satisfactory convergence is obtained. Typically we require the enthalpy profile to be converged within one or two percent depending on the degree of variation of the surface heat flux quantities.

Section 3
RADIATION TRANSPORT

We consider in this section the analysis underlying the calculation of the radiative flux F and the flux divergence term Q which appears in the energy equation. Transport expressions are derived for a one-dimensional planar geometry with the gas in local thermodynamic equilibrium. Primary emphasis is placed on the handling of discrete (i.e., line) absorption processes in the transport equation. The importance of atomic lines is now well recognized as a result of earlier investigations (Refs. 5, 15) of radiative transport in plasmas. Transport due to continuous absorption processes by atomic species is also included.

3.1 BASIC TRANSPORT EQUATIONS

The flux and flux divergence are given by*

$$F(y) = \int_0^\infty \int_{\omega=4\pi} I(y,\nu,\omega) \cos\theta \, d\omega \, d\nu \tag{41}$$

and

$$Q \equiv \nabla\cdot F(y) = \int_0^\infty \int_{\omega=4\pi} \mu(y,\nu)\Big[I(y,\nu,\omega) - B(y,\nu)\Big] \, d\omega \, d\nu \tag{42}$$

where $I(y,\nu,\omega)$ is the monochromatic intensity at frequency ν and in the

*For convenience in notation we drop the prime superscript used in Section 2 to denote dimensional quantities.

direction ω. The angular integration in Eqs. (41) and (42) is carried out using the forward-reverse approximation due to Schwartzchild (Ref. 16). The intensity is divided into two angular groups: those rays passing in the positive direction from left to right through a plane of symmetry (i.e., a plane normal to the y axis in our one-dimensional planar geometry) and those rays passing in a negative direction from right to left. The forward-reverse approximation represents all rays in the positive direction by a single ray I^+ with an average direction cosine $1/\ell$ and all rays in the negative direction by a single ray I^- also with an average direction cosine $1/\ell$ (cf. Fig. 3)

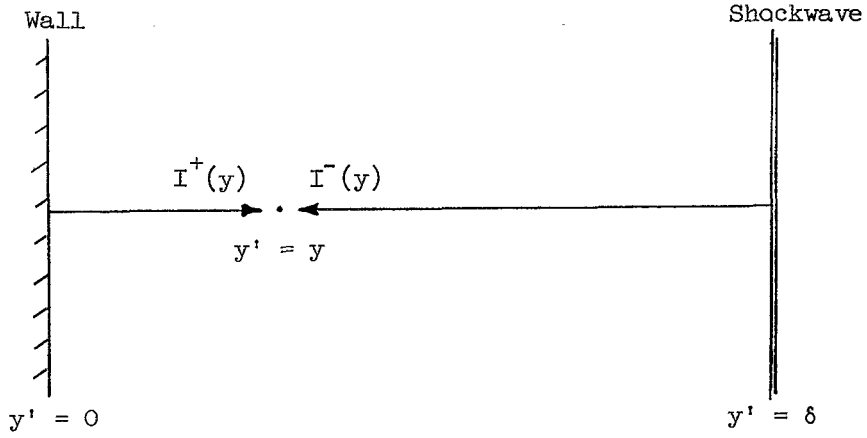

Fig. 3 Geometry for Radiative Transport in a One-Dimensional Planar Medium

As is well known, this two-stream approximation is equivalent to the exponential approximation to the exponential integral kernel function which arises in an exact formulation. An analysis of transport in a uniform gas (Ref. 17) shows that a value of $\ell = 2$ provides a good approximation to the exact flux and flux divergence values.

The monochromatic intensities I^+ and I^- are given by

$$I^+(\nu,y) = \int_o^y \mu(\nu,y')\, B(\nu,y')\, e^{-\ell\int_{y'}^{y} \mu(\nu,y'')\, dy''}\, dy' \tag{43a}$$

$$I^-(\nu,y) = \int_y^\delta \mu(\nu,y')\, B(\nu,y')\, e^{-\ell\int_{y}^{y'} \mu(\nu,y'')\, dy''} \tag{43b}$$

In carrying out the frequency integration in Eqs. (41) and (42), the absorption coefficient is separated into the continuum and line contribution.

$$\mu(\nu,y') = \mu^C(\nu,y') + \mu^L(\nu,y') \tag{44}$$

The flux may then be expressed as the sum of a contribution due to continuum only processes F^C and a contribution due to lines but corrected by continuum attenuation.

$$F(y) = F^C(y) + F^L(y) \tag{45}$$

For the continuum contribution we can formally express the flux in terms of integration over space and frequency.

$$F^C(y) = \pi \int_o^\infty \left\{ \int_o^{E(o,y)} B(\nu,y')\, dE_\nu(y',y) - \int_o^{E(y,\delta)} B(\nu,y')\, dE_\nu(y,y') \right\} d\nu \tag{46}$$

where the emissive function $E_\nu(y,y')$ is introduced to simplify the numerical spatial integrations,

$$E_\nu(y',y) = E_\nu\left[-(y,y')\right] = 1 - \exp\left[-\ell \int_{y'}^{y} \mu^C(\nu,y'')\, dy''\right] \qquad (47)$$

The frequency integration required by Eq. (47) will be considered in Section 3.2.

For the line contribution, the integration over frequency is carried out analytically for individual or groups of individual lines and the total contribution summed over all lines or groups of lines,

$$F^L(y) = \pi \sum_{\text{all lines } i} \int_o^{W_i(o,y)} B_i(y')\, dW_i(y',y) - \int^{W_i(y,\delta)} B_i(y')\, dW(y,y') \qquad (48)$$

where the frequency integration is incorporated into an equivalent width variable $W_i(y',y)$ defined as

$$W_i(y',y) = W_i\left[-(y,y')\right] = e^{-\ell\int_{y'}^{y} \mu_i^C(y'')dy''} \int_{\Delta\nu}\left[1-\exp(-\ell \int_{y'}^{y} \mu_i^L(\nu,y'')\, dy'')\right]d\nu \qquad (49)$$

In defining $W_i(y',y)$ in this manner we have assumed that the Planck function and continuum absorption are frequency independent (at least approximately) over the interval $\Delta\nu$. The evaluation of the frequency integration required by Eq. (49) will be considered in Section 3.3.

In a similar manner, we treat the flux divergence as due to a continuum only

contribution and terms due to lines plus continuum. Due to cross terms there are a total of four contributions (Ref. 17).

$$Q \equiv \nabla \cdot F = Q^{C,C}(y) + Q^{C,L}(y) + Q^{L,C}(y) + Q^{L,L}(y) \tag{50}$$

These Q terms are defined as

(1) the energy emitted and absorbed by the continuum;

$$Q^{C,C}(y) = 2\pi \int_o^\infty \mu^C(y) \left\{ \int_o^{E_\nu(o,y)} B(\nu,y')\, dE_\nu(y,y') + \int^{E_\nu(y,\delta)} B(\nu,y')\, dE_\nu(y',y) - 2B(\nu,y) \right\} d\nu \tag{51}$$

(2) the energy emitted by the continuum and absorbed by the lines;

$$Q^{C,L} = 2\pi \sum_{\text{all lines, } i} \int_o^{E_\nu(o,y)} B_i(y') \left[S_i(y) - A_i(y',y) \right] dE_\nu(y',y) + \int_o^{E_\nu(y,\delta)} B_i(y') \left[S_i(y) - A_i(y,y') \right] dE_\nu(y,y') \tag{52}$$

(3) the energy emitted by lines and absorbed by the continuum;

$$Q^{L,C} = 2\pi \sum_{\text{all lines, } i} \mu_i^C(y) \int_o^{W_i(o,y)} B_i(y')\, dW_i(y',y) + \int_o^{W_i(y,\delta)} B_i(y')\, dW_i(y,y') \tag{53}$$

(4) the energy absorbed and emitted by lines,

$$Q^{L,L} = 2\pi \sum_{\text{all lines, } i} \int_{o}^{A_i(o,y)} B_i(y') \, e^{-\ell \int_{y'}^{y} \mu_i^C(d'')dy''} \, dA_i(y',y)$$

$$+ \int_{o}^{A_i(y,\delta)} B_i(y') \, e^{-\ell \int_{y}^{y'} \mu_i^C(y'')dy''} \, dA_i(y,y') - 2B_{\nu_i}(y) \, S_i(y) \qquad (54)$$

In Eqs. (52) and (54) the frequency integration is performed in terms of an absorption equivalent width variable $A_i(y',y)$ defined as

$$A_i(y',y) = A_i\left[-(y,y')\right] = \int_{\Delta\nu} \mu_i^L(\nu,y)\left[1-\exp(-\ell \sum_i \int_{y'}^{y'} \mu_i^L(\nu,y'')dy'')\right]d\nu \qquad (55)$$

3.2 TREATMENT OF THE CONTINUUM PROCESSES

The continuum absorption coefficient varies relatively slowly as compared, say, to the line absorption coefficient (except in the neighborhood of photoionization edges). Hence a monochromatic evaluation of the flux and flux divergence at selected frequencies followed by numerical quadrature over frequencies is practical. However, with the aid of a few approximations we can reduce, considerably, the computational effort required in the monochromatic approach. First we will neglect the role of molecular absorption. The effect of this approximation will be examined in Section 5.* For the atomic species H, C, N, and O we note from past experience that, for shock layer pressures and thickness of interest (for values of the product $p \cdot R \leq 500$ atm cm), at

*In the multi-group frequency model which follows, molecular band absorption could be included by adding additional frequency groups.

frequencies below the first major photoionization edge, the shock layer is optically thin. For frequencies above the photoionization edge, the absorption coefficient is essentially constant (Ref. 18). Hence we can represent the frequency dependent absorption coefficient by a series of grey absorption coefficients. For the first optically thin spectral group the appropriate grey absorption coefficient is the partial Planck mean,

$$\mu_P = \frac{\int_{\Delta\nu} \mu(\nu,T,\rho)\, B(\nu,T)\, d\nu}{\int_{\Delta\nu} B(\nu,T)\, d\nu} \tag{56}$$

and

$$\mu(\nu,T,\rho) = \sum_i \mu_i^C(\nu,T,\rho) = \sum_i N_i \sigma_i(\nu,T,\rho)(1-e^{-h\nu/kT}) \tag{57}$$

where $\mu_i(\nu,T,\rho)$ is the continuous absorption cross section for each specie (H, C, N, O) considered.* Note that for each specie the absorption coefficient has the same form (Ref. 18)

$0 \le h\nu \le h\nu_T^i$

$$\sigma_i = 7.26^{-16}\, \Gamma_i\, kT\, e^{-\left(\frac{\epsilon_i - h\nu - \Delta}{kT}\right)} \frac{\xi_i(h\nu)}{(h\nu)^3} \tag{58a}$$

$h\nu > h\nu_T^i$

$$\sigma_i = 7.26^{-16}\, \Gamma_i\, kT\, e^{-\left(\frac{\epsilon_i - h\nu_T^i}{kT}\right)} \frac{\xi_i(h\nu)}{(h\nu)^3} \tag{58b}$$

*We neglect the contribution from ionic species which is unimportant for shock layer temperatures $T \le 20{,}000\ ^{o}K$.

where in Eqs. (58a) and (58b)

Γ_i = specie statistical weight factor

ϵ_i = specie ionization energy

Δ = photoionization edge shift

$h\nu_T$ = merged energy level limit

ξ_i = nonhydrogenic correction factor

For the remaining frequency groups which lie above the first major photoionization edge, the cross section is chosen as a constant appropriate to the summed contribution from H, C, N and O atoms. The detailed expressions for the continuum absorption coefficient used in the calculations are given in Appendix A. In terms of the grey absorption coefficient, the flux and flux divergence expression for each group k becomes

$$F_k = \pi \int_o^{E_k(o,y)} B_k(y')\, dE_k(y',y) - \int_o^{E_k(y,\delta)} B_k(y')\, dE_k(y,y') \tag{59}$$

$$Q_k^{C,C}(y) = 2\pi\, \mu_k^C(y) \left[\int_o^{E_k(o,y)} \bar{B}_k(y')\, dE_k(y',y) + \int_o^{E_k(y,\delta)} B_k(y')\, dE_k(y,y') - 2\bar{B}_k \right] \tag{60}$$

where

$$\bar{B}_k = \int_{\Delta\nu_k} B(\nu,T)\, d\nu \tag{61}$$

and E_k is obtained from Eq. (47) using the grey absorption coefficient $\mu_k^C(y')$.

3.3 TRANSPORT FOR A SINGLE ISOLATED LINE

We will consider in this subsection the contribution to the flux and flux divergence due to a single, isolated line. For the thermodynamic conditions of interest, an isolated line has a Lorentzian shape characterized by a strength S and (half) half-width γ determined by electron impact,*

$$\mu^L(\nu) = \frac{S(y'')\ \ (y'')}{\pi}\left[\frac{1}{(\nu-\nu_o)^2+\ \gamma^2(y'')}\right] \tag{62}$$

where

$$S(y'') \equiv \int_o^\infty \mu^L(\nu)d\nu = \frac{\pi e^2}{mc}\, N_n(y'')\ f_{nn'}(1-e^{-h\nu_o/kT}) \tag{63}$$

In Eq. (63) N_n is the number density of the lower state and $f_{nn'}$ the f-number** determining the transition probability strength.

For transport within a homogeneous gas (i.e. one having a constant thermodynamic state), the frequency integration required by the equivalent width variables $W(y,y')$ and $A(y,y')$ is readily performed (see, for example, Ref. 19)). For the nonhomogeneous case, the spatial dependence of the half-width $\gamma(y'')$ in the denominator of Eq. (62) precludes a closed-form evaluation of the required frequency integration. In order to avoid prohibitively costly numerical frequency integrations, it is necessary to replace the actual

---

*In general, $\mu^L(\nu)$ should include, in the denominator of Eq. (62), a line shift. This shift, however, can be neglected in treating transport problems.

**That is, the f-number appropriate to a single line, or multiplet, or whatever collection of line transitions is represented by the lower state number density N_n.

spatially dependent half-width $\gamma(y'')$ (again only in the denominator of Eq. (62)) by a spatially averaged value $\bar{\gamma}$. Note that for optically thick situations (more precisely, situations where the line center is optically thick over a spatial extent for which the temperature is nearly uniform) transport occurs essentially in the line wings. Under this condition, the value of $\gamma(y'')$ in the denominator of Eq. (62) is unimportant. It is shown in Ref. 20 that best compromise to use in selecting the spatially averaged value for $\gamma(y'')$ is to define $\bar{\gamma}$ such that in the optically thin limit the correct flux value is obtained. Let us determine this value.

Consider the spatial integral appearing $W(y,y')$ and $A(y,y')$, Eqs. (49) and (55),

$$Z = \ell \int_{y'}^{y} \mu^{L}(\nu,y'')\, dy'' \tag{64}$$

Define a transport variable

$$z = \frac{\ell}{\pi} \int_{y'}^{y} S(y'')\gamma(y'')\, dy'' \tag{65}$$

then using Eq. (62) and approximating $\gamma(y'')$ in the denominator by $\bar{\gamma}(z)$, we rewrite Eq. (64) as

$$Z = z\left[\frac{1}{(\nu-\nu_o)^2+\bar{\gamma}^2(z)}\right] \tag{66}$$

where $\bar{\gamma}^2(z)$ is yet to be determined. We emphasize that, while $\bar{\gamma}(z)$ is

taken as constant over the interval y', y, $\bar{\gamma}(z)$ is not constant over the entire layer $(0 \leq y \leq \delta)$ but rather depends both on the value of y and the running variable y'. Using this average half-width approximation, we obtain the following expressions for $W(z)$ and $A(z)$ (Ref. 20),*

$$W(z) = 2\pi \bar{\gamma}\, t\, e^{-t} \left[I_o(t) + I_1(t) \right] \tag{67}$$

$$A(z) = S(y) \left[1 - e^{-t}\, I_o(t) \right] \tag{68}$$

where

$$t = \frac{z}{2\bar{\gamma}^2} \tag{68a}$$

and I_o and I_1 are the modified Bessel functions of the first kind. Considering first the equivalent width variable W which appears in the flux calculation, it is clear that W is independent of $\bar{\gamma}$ in the limit $t \gg 1$. Then in order to obtain the correct optically thin expression in the limit $t \ll 1$, viz.

$$W = \int_{y'}^{y} S(y'')\, dy'' \tag{69}$$

we require

$$\bar{\gamma}(z) = \frac{\int_{y'}^{y} S(y'')\gamma(y'')\, dy''}{\int_{y'}^{y} S(y'')\, dy''} \tag{70}$$

---

*For the purposes of this discussion we will omit the continuum attenuation factor appearing in Eq. (49) in writing down the results for W. It is clear that the complete equivalent width is obtained by multiplying Eq. (67) by the continuum factor.

For the flux divergence equivalent width calculation, one can show (Ref. 20) that the appropriate value for $\bar{\gamma}$ is the value at the local point at which $\nabla \cdot F$ is being calculated, i.e. $\bar{\gamma} = \gamma(y)$. This completes the analysis for the case of a single isolated line.

3.4 TRANSPORT FOR A COLLECTION OF ISOLATED LINES*

In our calculations of the flux and flux divergence, we shall deal with a "group" of lines defined as a collection of adjacent lines within a spectral interval across which both the Planck function and continuum absorption coefficient can be approximated as being independent of frequency. For the moment we consider the situation in which the lines within the group are non-overlapping. Then Eq. (48) gives the total flux from all lines in the group if we interpret $W(y,y')$ as the sum of the equivalent width of each individual line,

$$W(y,y') = \sum_{m=1}^{n} W_m(y,y') \tag{71}$$

where n is the total number of lines in the group. Our objective is to approximate the summation required by the right-hand side of Eq. (71) with a single expression of the form

$$\sum_{m=1}^{n} W_m(y,y') = n\, W(S^*,\gamma^*) \tag{72}$$

where S^* and γ^* are line parameters appropriately averaged over all lines

*As in the continuum case we shall be considering systems containing a mixture of H, C, N and O atoms. We shall include only neutral atom transitions, the contribution from the ionic lines being negligible.

in the group. If we make the assumption that all lines within the group are either optically thin or optically thick (i.e. there does not exist a mixed collection of thin and thick lines) we can derive expressions defining S^* and γ^*. This uniformly thin or thick line assumption is reasonable since most of the lines within a group arise from similar transitions. In any event, the accuracy of this basic assumption will be checked by comparison with detailed line-by-line calculations in Section 5.

For the optically thin limit the two sides of Eq. (72) reduce to

$$\sum_m \int_{y'}^{y} S_m(y'')\, dy'' = n \int_{y'}^{y} S^*(y'')\, dy'' \tag{73}$$

which requires

$$S^* = \frac{1}{n} \sum_m S_m \tag{74}$$

For the optically thick limit the two sides of Eq. (72) reduce to

$$\sum_m 2 \left[\int_{y'}^{y} S_m(y'')\, \gamma_m(y'')\, dy''\right]^{1/2} = n \left[\int_{y'}^{y} S^*(y'')\, \gamma^*(y'')\, dy''\right]^{1/2} \tag{75}$$

Due to the non-linear square root operator in Eq. (75) we must make the following approximation to proceed further,

$$\left\{\sum_m \left[\int_{y'}^{y} S_m(y'')\gamma_m(y'')\, dy''\right]^{1/2}\right\}^2 \approx \int_{y'}^{y} \left\{\sum_m \left[S_m(y'')\gamma_m(y'')\right]^{1/2}\right\}^2 dy'' \tag{76}$$

If the spatial variation of the $S_m\gamma_m$ product is the same for all lines (differing only by a constant factor) then Eq. (76) holds. The half-width γ_m is proportional to the electron number density,

$$\gamma_m(y'') = \beta_m \, Ne(y'') \tag{77}$$

where β_m is a constant (i.e. a normalized half-width). The line strength is proportional to the lower state number density and the induced emission factor,

$$S_m(y'') = 1.10^{-16} \, f_m \, N_m(y'') \left[1 - e^{-h\nu/kT(y'')}\right] \tag{78}$$

Then under the condition that all lines within the group have a common lower state, Eq. (76) is exact. Proceeding on that basis, Eqs. (75) and (76) yield,

$$\gamma^* = \frac{1}{n^2 S^*} \left\{ \sum_m \left[S_m \gamma_m \right]^{1/2} \right\}^2 \tag{79}$$

We note in passing that a similar treatment of the flux divergence equivalent width function A leads to an identical expression for γ^*.

Within a group we have, in general, line transitions involving all four species being considered (H, C, N and O neutral atoms). Hence the expression for the effective half-width, Eq. (79), is not valid if we lump all lines within the group together. Indeed, for the shock layer problem with mass injection the spatial variation of the number density of the various atomic species varies drastically and the approximation of Eq. (76) is quite poor if we lump lines of differing species together. However, for a given atomic species, lines lying

in the same spectral group do arise from either the same or nearby lower states and hence for a given atomic species the approximation of Eq. (76) is reasonable. Then we propose a model in which for each line group we calculate the equivalent width for all lines of a given atom. The total equivalent width for all lines of the group becomes,

$$\sum_{m=1}^{n} W_m(y,y') = \sum n_i W_i(S_i^*,\gamma_i^*) \tag{80}$$

where $W_i(S_i^*,\gamma_i^*)$ is the lumped equivalent width for each atom and where n_i, S_i^*, γ_i^* refer to the effective line parameters for that atom. The quantities S_i^*, γ_i^* are calculated from Eqs. (74) and (79) where the summation now includes only those lines for a given atomic specie. Using the expressions for the half-width and line strength, Eqs. (77) and (78), we find that these quantities can be expressed as

$$S_i^*(y'') = 1.10^{-16}\, N_i(y'')\left[1-e^{-h\nu/kT(y'')}\right] f_i^* \tag{81}$$

$$\gamma_i^*(y'') = N_e(y'')\, \beta_i^* \tag{82}$$

where $N_i(y'')$ is the total number density of the given atomic specie i. The f_i^* and β_i^* are calculable in terms of the basic f-numbers and normalized half-widths for each specie. The equations for f_i^*, β_i^* are

$$f_i^* = \sum_m \frac{f_m\, g_m\, e^{-\epsilon_m/kT}}{\Sigma_i} \tag{83}$$

$$\beta_i^* = \frac{1}{n_i^2 f_i^*} \sum_m \left[\frac{f_m \beta_m g_m \, e^{-\epsilon_m/kT}}{\Sigma_i} \right]^{1/2} \qquad (84)$$

where, again, the summation is over the lines of a given species.

Examination of the line spectrum for H, C, N, O atoms showed that the lines could be collected into nine groups. Within each group we consider four "effective lines," one for each atomic species, whose f-number and half-width f_i^*, γ_i^* are calculated from Eqs. (83) and (84). Hence we handle a total of 36 "lines" although the spatial integrals required to evaluate the flux and flux divergence expressions need only be performed for each of the nine groups. We tabulate in Appendix B, the pertinent properties of these nine line groups including spectral location, frequency interval covered and values of f_m and $(f_m \beta_m)^{1/2}$.

3.5 TREATMENT OF OVERLAPPING LINES

The analysis presented in subsection 3.4 assumed that the lines within the group were isolated. We consider here the correction to the group equivalent width obtained by this approach when overlapping occurs. The exact expression for the equivalent width for a collection of m lines within the group is (again omitting the continuum attenuation factor)

$$W_{group} = \int_D \left[1 - \exp - \sum_m \int_{y'}^{y} \mu_m^L (\nu, y'') \, dy'' \right] d\nu \qquad (85)$$

where the summation is over all lines and D is the spectral interval covered by the group.

Under the condition that all lines within the group are non-overlapping, the group equivalent width is simply the sum of the isolated line equivalent. widths W_m

$$W_{group} = W_I = \sum_m W_m \tag{86}$$

However, when the lines overlap, an analytic result for the frequency integration in Eq. (85) is not available even for the relatively simple case of just two overlapping lines (e.g. see Ref. 21). We are then forced to perform numerical integration when overlapping occurs. To carry out this frequency integration as part of a coupled radiative flow calculation is not feasible. Such an approach would significantly increase the computational time required in the radiative transport portion of the calculation; a portion which already accounts for roughly 50% of the total computational time. Instead we devised the method discussed below which empirically correlates the line group equivalent width for overlapping lines (as deteremined by numerical frequency integration) with a parameter which measures the amount of line overlapping within the line group.

The spectral interval D defining a particular line group is a fixed interval. Thus when thelines are optically thick and strongly overlapping within this interval, the line group equivalent width approaches the value of D . It is realized that under such an extreme condition of overlapping the contributions of the line wings from one line group to the absorption coefficient in adjacent line groups should be taken into account. Nevertheless, our line transport

model neglects this effect. This omission is not likely to yield a serious error since, when one line group exhibits such strong overlapping, the equivalent widths of adjacent line groups are often also approaching their asymptotic value D. Hence an additional absorption coefficient contribution from adjacent line groups would have only a small effect on the total transport. To emphasize, then, we account for overlapping only within the fixed spectral interval of each line group.

A means of measuring the amount of overlapping within a group is to compare the isolated line value W_I (as obtained from Eq. (86)) with the spectral interval D. When $W_I \ll D$ it is clear that the lines must be essentially isolated. On the other when W_I is of the order of D, then overlapping of lines must be occurring. Finally when $W_I \gg D$ a condition of nearly total overlapping occurs in which case the group equivalent width should be also equal to D. We postulate then that the variable

$$\alpha = W_I/D \tag{87}$$

is a universal measure of the degree of overlap and can be used to correlate values of the exact group equivalent width for various thermodynamic-pathlength conditions. To check this hypothesis, a set of calculations were made of the exact group equivalent width (as determined by numerical integration of Eq. (85)) for the spectral interval from $h\nu = 9.80$ eV to 10.80 eV in which 10 NI lines of various strengths and half-widths were located.*

* The f-numbers and γ values were taken from Ref. 18.

The group equivalent widths were evaluated for the following conditions: $p = 1$ atm and $T = 10{,}000^{\circ}K$; $12{,}000^{\circ}K$; $15{,}000^{\circ}K$; $17{,}000^{\circ}K$. For each thermodynamic condition, pathlengths ranging from 0.1 cm to 50 cm were considered. These results are given in Fig. 4a where we plotted W_{group}/D versus the correlation variable α defined above. It can be seen that the variable α does an admirable job of correlating the exact values. Also, we were able to fit these numerical results by the following function,

$$W_{group}/D = \left[\frac{2}{\pi} \tan^{-1} \left(\frac{\pi}{2} \alpha\right)\right] \tag{88}$$

For the flux divergence, the quantity effected by overlapping is

$$\Gamma(y,y') \equiv S(y) - A(y,y') = \int \mu^L(\nu,y)\, e^{-\int_{y'}^{y} \mu^L(\nu,y'')dy''} d\nu \tag{89}$$

which, for the group, becomes

$$\Gamma_{group} = \int_D \left\{ \sum_m \mu_m^L(\nu,y) \exp - \sum_m \int_{y'}^{y} \mu_m^L(\nu,y'')\, dy'' \right\} d\nu \tag{90}$$

For nonoverlapping lines we have

$$\Gamma_{group} = \Gamma_I = \sum_m \Gamma_m \tag{91}$$

We evaluated the quantity Γ_{group} by numerical integration of Eq. (90) for the same set of lines and the same thermodynamic-pathlength condtions used in evaluating W_{group} . The ratio Γ_{group}/Γ_I is plotted against the correlation variable α in Fig. 4b. Again we observe that the exact values of Γ_{group} are well correlated

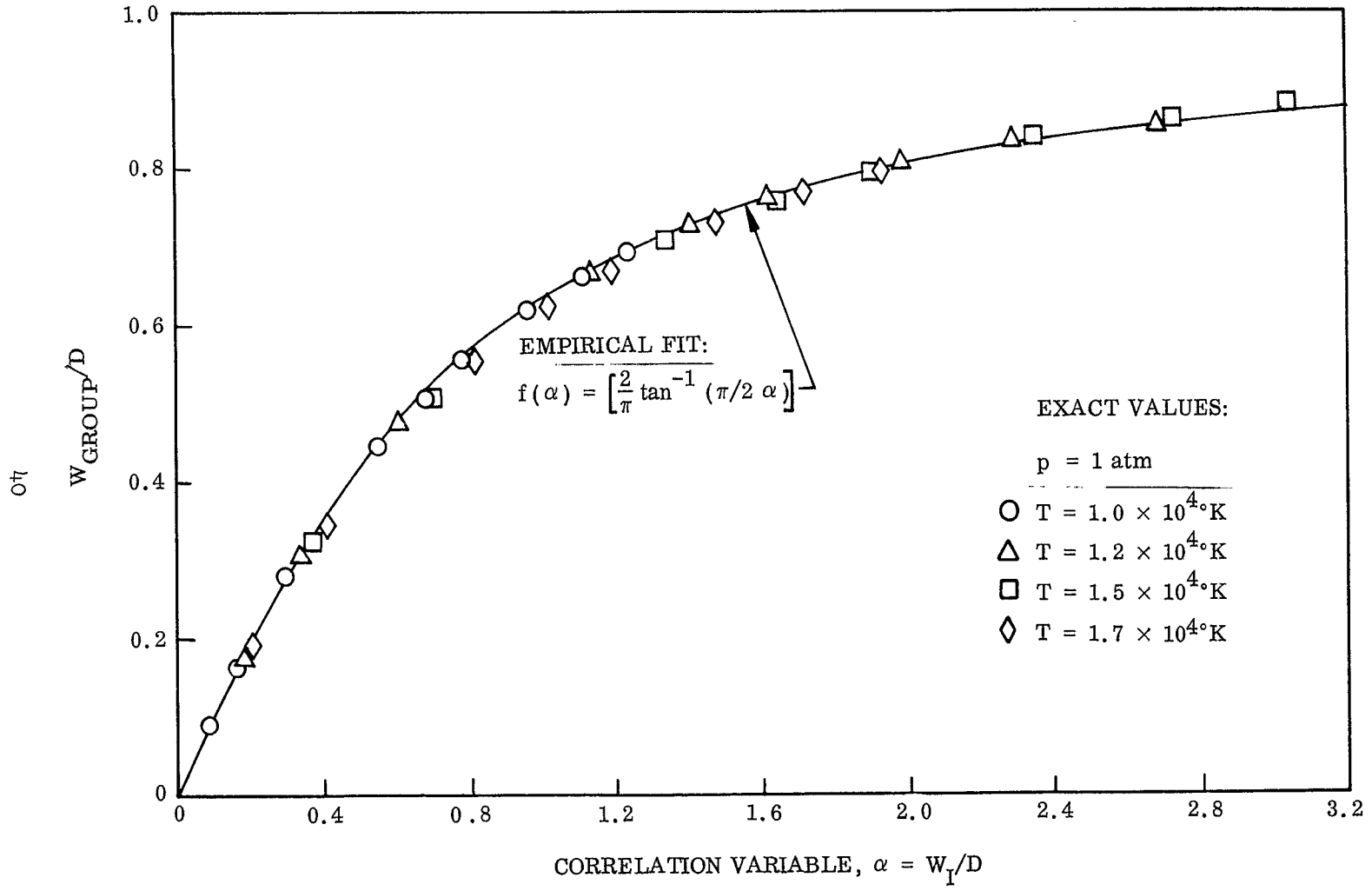

Fig. 4a Flux Overlap Function

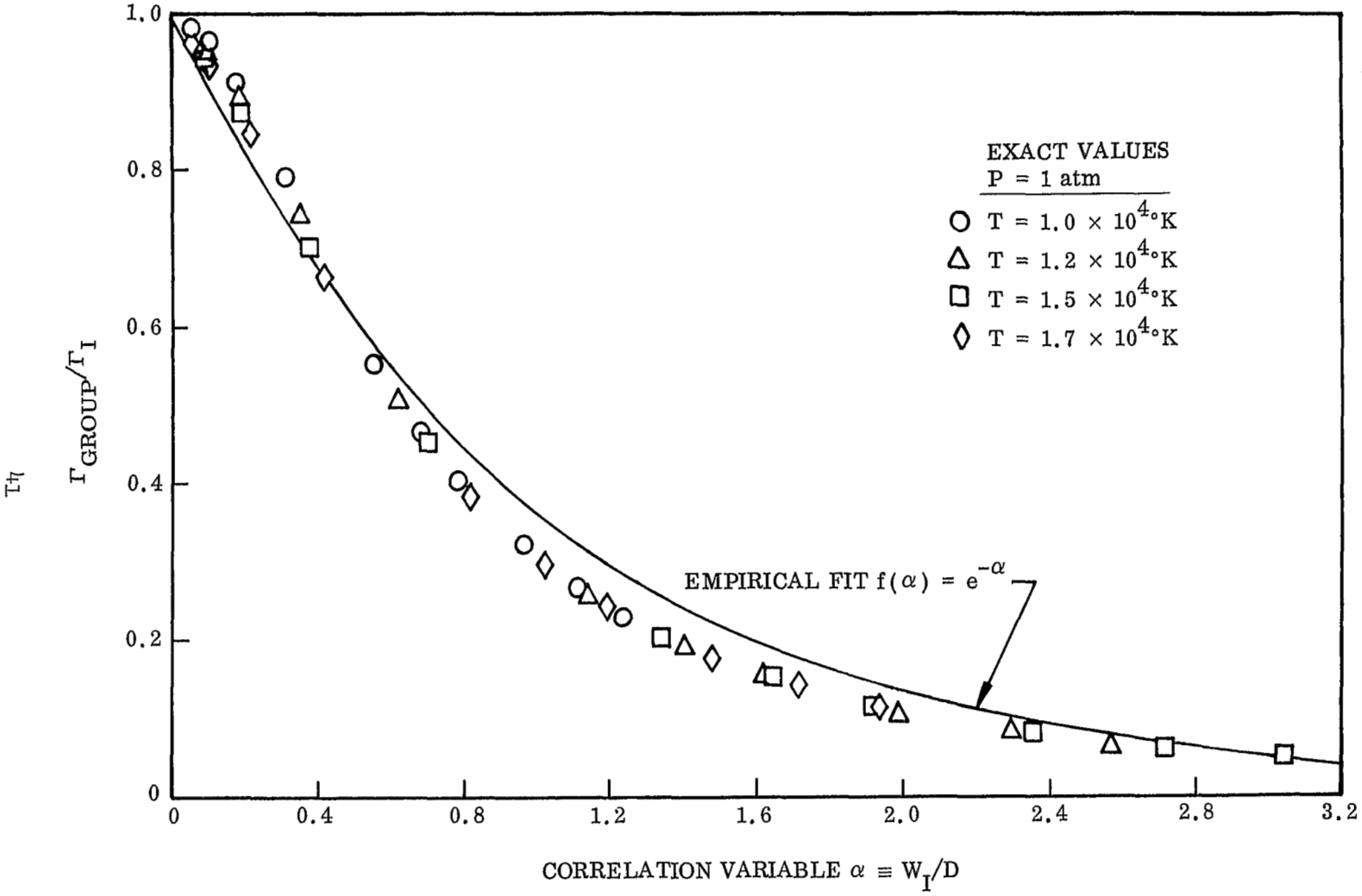

Fig. 4b Flux Divergence Overlap Function

by this variable α . The numerical values were fitted by the expression

$$\frac{\Gamma_{group}}{\Gamma_I} = e^{-\alpha} \tag{92}$$

In summary then the quantities W_{group} and Γ_{group} are obtained by first calculating the isolated line limiting values from the analysis of Section 3.4 and then using Eqs. (88) and (92) to correct for overlapping.

To assess the importance of line overlap, a calculation was made (using the shock layer temperature-pressure distribution obtained from the non-blowing coupled flow calculation discussed in Section 5) of the line transport with and without the line overlap correction. The results are summarized below:

Line Group Number	Spectral Interval (eV)	Flux - without overlap correction W/cm^2	Flux - including overlap correction W/cm^2
1	1.00 - 1.60	1.10×10^3	1.08×10^3
2	1.60 - 3.80	$.45 \times 10^3$	$.45 \times 10^3$
3	5.00 - 6.50	0	0
4	6.50 - 8.40	$.69 \times 10^3$	$.69 \times 10^3$
5	8.40 - 9.80	$.56 \times 10^3$	$.56 \times 10^3$
6	9.80 -10.80	2.34×10^3	1.11×10^3
7	10.80 -12.00	$- .09 \times 10^3$	$- .25 \times 10^3$
8	12.00 -13.40	$- .12 \times 10^3$	$- .09 \times 10^3$
9	13.40 -14.40	$- .04 \times 10^3$	$- .02 \times 10^3$
Total		4.90×10^3	3.53×10^3

We see that in terms of the total line flux, the overlap correction results in about a 30% reduction from a calculation without the overlap correction. Moreover, almost

all the correction occurs for line group 6 which is the spectral region for which we devised the empirical overlapping line correlation expression (although for simplicity the correlation equation was developed considering a set of NI lines only).

3.6 LOCAL SOLUTIONS FOR THE FLUX DIVERGENCE

The numerical evaluation of the line flux term given by Eq. (48) affords no particular numerical problems. One can construct a spatial mesh using a reasonable number of grid points (typically less than 50) for which the integrand in Eq. (48) (i.e. the Planck function) changes only slightly. A similar statement applies to the flux divergence terms $Q^{L,C}$ and $Q^{C,L}$. However, the evaluation of $Q^{L,L}$ presents special difficulties for the case of optically thick lines. Let us rewrite $Q^{L,L}$ given by Eq. (54) as*

$$Q^{L,L} = 2\pi \int_{A(\Delta y^-)}^{A(o,y)} B(y')dA(y,y') + 2\pi \int_{A(\Delta y^+)}^{A(y,\delta)} B(y'')dA(y',y)$$

$$+ Q^{L,L,-}_{local} + Q^{L,L,+}_{local} \qquad (93)$$

where

$$Q^{L,L,-}_{local} = 2\pi \left[\int_o^{A(\Delta y^-)} B(y')\ dA(y,y') - S(y)\ B(y) \right] \qquad (94)$$

$$Q^{L,L,+}_{local} = 2\pi \left[\int_o^{A(\Delta y^+)} B(y')\ dA(y',y) - S(y)\ B(y) \right] \qquad (95)$$

* For convenience we will omit the continuum attenuation term. It can be included in an approximate manner where necessary.

Let us consider $Q^{L,L,-}_{local}$. Difficulty arises when, for a line which is very optically thick, $\Delta A^- \to S(y)$. Under these circumstances, replacing $B(y')$ by its average value, viz.

$$\bar{B} = \frac{B(y) + B(\Delta y^-)}{2} \tag{96}$$

leads to significant error. The correct solution is found by evaluating the integral in Eq. (94) by parts which yields

$$Q^{L,L,-}_{local} = B(\Delta t^-)\, A(\Delta t^-) - \int_o^{\Delta t^-} A(t)\, \frac{dB}{dt}\, dt \tag{97}$$

where we have introduced the transport variable t defined by Eq. (68a). We now replace dB/dt by a constant

$$\frac{dB}{dt} = \frac{B(\Delta t^-) - B(o)}{\Delta t^-} \tag{98}$$

and we obtain

$$Q^{L,L,-}_{local} = - B(\Delta t^-)\, \Gamma(\Delta t^-) + \left[B(\Delta t^-) - B(o)\right] \Lambda(\Delta t^-) \tag{99}$$

where

$$\Gamma(\Delta t^-) = S(o) - A(\Delta t^-) = e^{-\Delta t^-/2}\, I_o(\Delta t^-/2) \tag{100}$$

and

$$\Lambda(\Delta t^-) \equiv \int_o^{\Delta t^-} A(t)dt = e^{-\Delta t^-/2} \left[I_o(\Delta t^-/2) + I_1(\Delta t^-/2)\right] \tag{101}$$

Equation (99) provides the correct limiting form for the flux divergence for the case of very large optical depth, $\Delta t^- \gg 1$. An analogous equation for $Q^{L,L,+}_{local}$ may be derived.

Section 4
THERMODYNAMIC AND TRANSPORT PROPERTIES

4.1 THERMODYNAMIC PROPERTIES

In order to obtain solutions to the conservation equations and the radiative flux and flux divergence expressions, state relations are required. The method of solution (cf. Sec. 2.4) is such that, given values of the enthalpy and pressure, the density and temperature are to be determined. Due to mass injection of gases containing hydrogen and carbon species, the elemental composition of the shock layer gases varies from point to point. This variable element problem is handled by performing, at each shock layer point, a complete thermochemical equilibrium composition calculation. The input data required are the mass fractions C_i of hydrogen, carbon, nitrogen, and oxygen atoms, the enthalpy (cal/gm) and the pressure (atm). The analysis underlying this thermochemical calculation* is described in Ref. 22. A user's description of the detailed input required including the basic thermodynamic data for each specie is given in Ref. 23.

Due to requirements on the specification of certain base species (cf. Refs. 22 and 23) it becomes necessary to separate the computation into a high temperature region (containing charged species) and a low temperature region (neutral species only). We list in Table 1 the various species considered in each

*This calculation is a separate computer program, the LMSC Free Energy Minimization Program (FEMP) which we have incorporated as a subroutine.

TABLE I

SPECIES DATA FOR FEMP CODE

Temperature Regime	Specie	Energy of Formation (cal/mole)	Temperature (°K) Range of Validity For Thermodynamic Data
LOW	CN	9.215^{+3}	1000-15000
	C_2	0	1000-12000
	O_2	0	1000-6000
	N_2	0	1000-24000
	H	5.162^{+4}	1000-16000
	O	5.8985^{+4}	1000-24000
	C	7.058^{+4}	1000-24000
	N	1.125^{+5}	1000-24000
	C_2H	-8.13^{+4}	1000-6000
	C_3H	-1.699^{+5}	1000-6000
	C_4H	-2.42^{+5}	1000-6000
	HCN	-6.7709^{+4}	1000-6000
	C_2H_2	-2.42^{+5}	1000-6000
	H_2	0	1000-6000
	CO	-1.262^{+5}	1000-6000
HIGH	e^-	0	2500-24000
	C	7.058^{+4}	1000-24000
	H^+	3.65138^{+5}	2500-24000
	CN	9.215^{+3}	1000-15000
	N	1.125^{+5}	1000-24000
	O^+	3.73033^{+5}	2500-24000
	N^+	4.48051^{+5}	2500-24000
	O	5.8985^{+4}	1000-24000
	N_2	0	1000-24000
	CO	-1.262^{+5}	2500-12000
	C^+	3.3083^{+5}	2500-24000
	H	5.162^{+4}	1000-16000

temperature regime along with the energy of formation* and the applicable temperature range of the individual specie thermodynamic data.

The condition for switching from low to high region in the FEMP calculation is not critical since there is a temperature range of common validity. For convenience we use a criteria based on the value of the molecular weight ratio

$$M_o/M\ (T,\rho,\alpha_i)$$

where M_o is the molecular weight at $p = 1$ atm $T \sim 1{,}000\ ^oK$.

4.2 TRANSPORT PROPERTIES

A full calculation of the transport properties for the multicomponent ablation product-air mixture is prohibitively complex for this investigation. The simplified transport equations of Refs. 24 and 25 have therefore been used. Blake (Ref. 26) illustrated the utility of these simplified equations in describing the transport coefficients of air (viscosity and Prandtl number) to temperatures of 10,000 ^oK. For the non-air systems, i.e. mass injection of C and H, the multicomponent system was assumed to be an effective binary mixture so far as diffusion is concerned. Consequently, the same simplified equations were utilized in the non-air systems although no confirmation of these results is available.

---

*FEMP uses a scheme in which the basic diatomic molecular specie of each element (H_2, C_2, N_2, O_2) is taken as having zero energy at 0 ^oK.

The approximate viscosity of a gas mixture is given by

$$\mu_m = \sum_{i=1}^{\nu} \frac{x_i \mu_i}{\sum_{j=1}^{\nu} x_j \Phi_{ij}} \tag{102}$$

where x_i is the mole fraction and μ_i is the viscosity of the species i, and

$$\Phi_{ij} = \frac{1}{2\sqrt{2}} \left(1 + \frac{M_i}{M_j}\right)^{-1/2} \left[1 + \left(\frac{\mu_i}{\mu_j}\right)^{1/2} \left(\frac{M_j}{M_i}\right)^{1/4}\right]^2 \tag{103}$$

The form of this semi-empirical equation is obtained from the rigorous kinetic theory of multicomponent gas mixtures (Ref. 27) by assuming the collision integral ratio A_{ij}^* (Ref. 24) to be equal to 5/3 and the binary diffusion coefficient is that for a rigid sphere gas (Ref. 28). Since for most gaseous mixtures A_{ij}^* does not equal 5/3 the constant $1/2\sqrt{2}$ appearing in Eq. (102) was determined by correlating with experimental data of gas mixtures near room temperature. For air, Blake (Ref. 26) showed that when compared with the more complete analysis of Yos (as taken from Ref. 29), Eq. (102) was applicable to 10,000 $^{\circ}$K when curve fits of the individual species viscosities (Ref. 30) were used.

In order to simplify the calculation of the total thermal conductivity of a gas mixture, the diffusion of the species was assumed to be that given by an effective binary mixture as suggested by Lees (Ref. 12). For such a system, the total thermal conductivity can be written as

$$k_T = k_{f_m} + \sum_{i=1}^{\nu} D\, h_i \frac{\partial C_i}{\partial T} \tag{104}$$

where k_{f_m} is the thermal conductivity due to molecular collision with no chemical reactions (frozen state), h_i is the enthalpy of the i^{th} species,

$$h_i = \int_{T_o}^{T} C_{p_i}\, dT + h_i \tag{105}$$

C_i is the mass fraction of species i and D is the effective binary diffusion coefficient of the system. In this form, the thermal conductivity can thus be identified as the sum of the effects of molecular collision (frozen) and enthalpy transport. The energy transport of a multicomponent mixture of polyatomic molecules due to molecular collisions, k_{f_m}, is often divided into that energy associated with molecular translation and an Eucken correction for the internal molecular energy modes, rotation and vibration. From the rigorous theory for gas mixtures, Hirshfelder, Mason and Saxena (Ref. 25) showed that the total energy transport of molecular collisions can be approximated by an equation similar in form to the simplified viscosity, Eq. (102),

$$k_{f_m} = \sum_{i=1}^{\nu} \frac{x_i k_i}{\sum_{j=1}^{\nu} x_j \Phi_{ij}} \tag{106}$$

where k_i is the frozen conductivity of the species i and, again, Φ_{ij} is given by Eq. (103).

The equilibrium compositions and thermodynamic properties of the gas mixtures are determined by the method of Section 4.1. The species concentration derivative $\partial C_i/\partial T$ is determined from the calculation outlined in Ref. 26. The effective diffusion coefficient is taken as the value for the binary diffusion of N_2 - N (Ref. 30). With these data the total thermal conductivity of Eq. (104) was determined for the air systems as a function of temperature. The results (Ref. 26) were within 15% of the more complete analysis of Yos (as taken from Ref. 29) for temperatures below 14,000 ^{o}K.

The specific heat at constant pressure of the mixture, C_{p_m}, was determined from the summation

$$C_{p_m} = \sum_{i=1}^{\nu} \left(\bar{C}_{p_i} + h_i \frac{\partial C_i}{\partial T} \right) \tag{107}$$

where $\bar{C}_{p_i}$ is the frozen specific heat of each species. In Ref. 26, heat values from Eq. (107) were shown to agree well with the results of Predvoditelev (Ref. 31) and Yos' data given in Ref. 29.

Figure 5, taken from Ref. 26, shows the comparison of Prandtl numbers as determined by Hansen (Ref. 32), Yos (taken from Ref. 29) and the simplified Eqs. (102)-(107). The Yos results are considered more complete in that they include all particle interactions whereas the Hansen data are based on three body interactions.

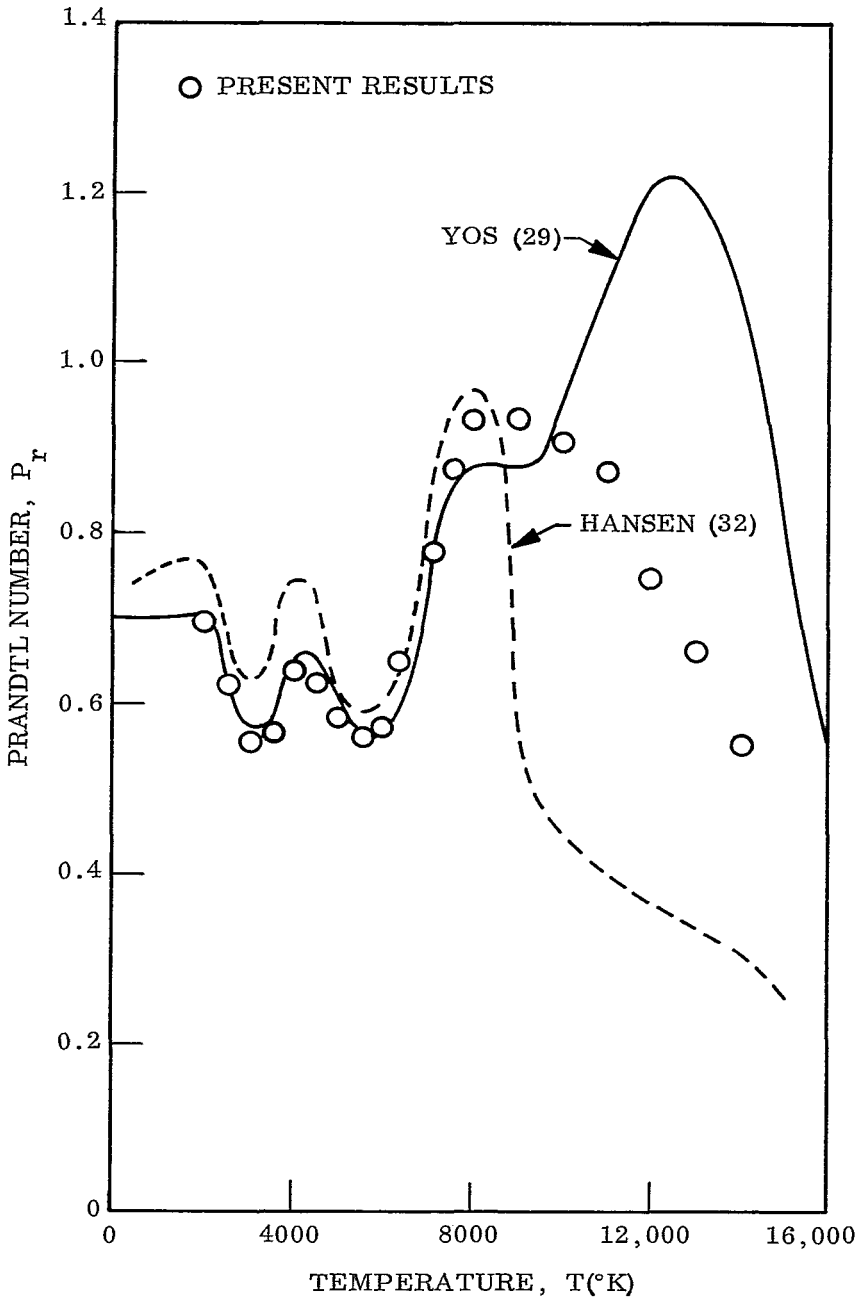

Fig. 5 Prandtl Number Comparison

Section 5
RESULTS

We discuss first in this section the comparison between the current detailed solution to the differential momentum equations and the previous integral method results. Next we demonstrate the validity of the radiative transport model developed in Section 3. Our current results for the radiative and convective heating rates are compared with those of a number of authors. Finally we present an investigation of the effectiveness of ablation product gases of predominantly hydrogen and carbon composition in absorbing the radiant energy from the high temperature air region.

5.1 COMPARISON WITH OTHER SOLUTIONS

To assess the significance of the $\rho\mu$ = constant approximation on the velocity field solution, we have compared our calculations with those of Howe and Viegas, Fig. 3 of Ref. 1. The flight conditions for this case are:

U_∞ = 15.24 km/sec 50,000 Ft.

$\rho_\infty = 4.63^{-7}$ gm/cm^3

alt ~ 58 km 190 Kft

R = .305 m 1 Ft

As shown by the comparison in Fig. 6, our solution is fairly close to the more exact solution of Howe and Viegas in the viscous layer where transport effects are felt. The maximum difference is about 25% and this much error occurs only for a small region.

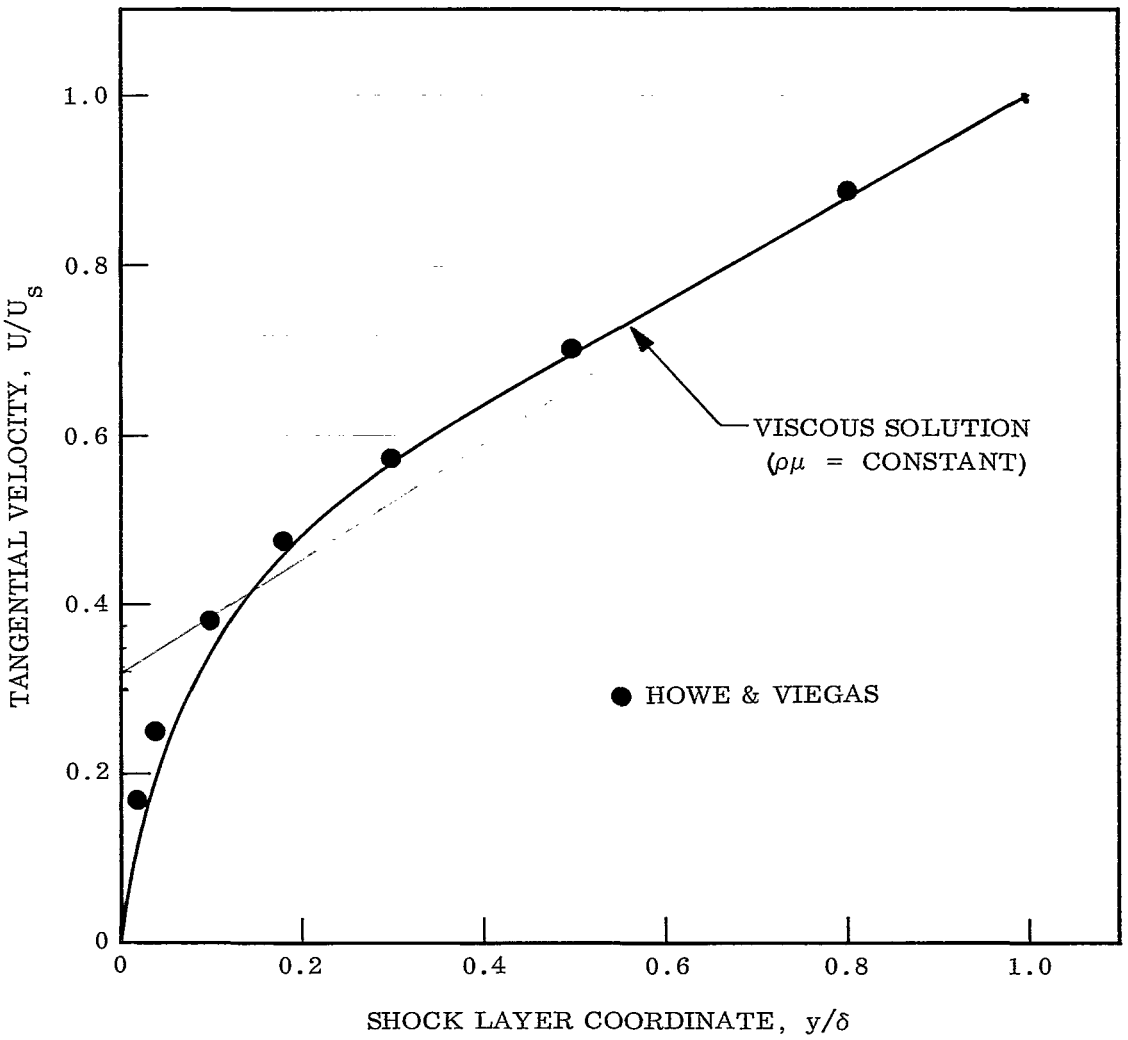

Fig. 5.1

Fig. 6 Evaluation of the Approximation $\rho\mu$ = constant in the Tangential Velocity Distribution

The integral-method solution to the momentum equation previously applied to the stagnation point shock layer problem was felt adequate for Reynolds number not too large ($Re_\delta \lesssim 10^6$) and for very low mass injection levels ($f_w \ll 1$). However, for large Reynolds numbers or high mass injection rates, the ability of the integral-method to produce the resulting steep velocity gradients was questionable. It is of interest then, to compare our current solution using the full differential equations with the older method. This is done in Figs. 7 and 8. In Fig. 7 we compare a non-blowing solution for a set of flight conditions yielding $Re_\delta = 4.1 \times 10^6$. The differences are larger than anticipated. Particularly noticeable is the change in the wall velocity gradient, which increased the convective heating by 40% and brought the new results for the convective heating into close agreement with boundary layer theory. In Fig. 8 we compare results for a case with large blowing, $f_w = 1.56$. Here the old two-layer integral solution, as expected, is quite inadequate. In making the comparisons shown in Figs. 7 and 8, we have used the same enthalpy distribution in each case for both momentum equation solutions in order to isolate the effects of the integral and differential treatment. It is clear the current method, being considerably more accurate, is well worth the added numerical complexity.

In Section 3 we introduced our continuum and line transport models, the development of which required various approximations. The validity of these models is best determined by comparing the radiative flux values with a calculation free from their essential approximations. Such a more exact calculation is afforded by our radiation transport code (RATRAP)* in which the continuum contribution is

*The analysis underlying this radiation transport code is given in Ref. 20.

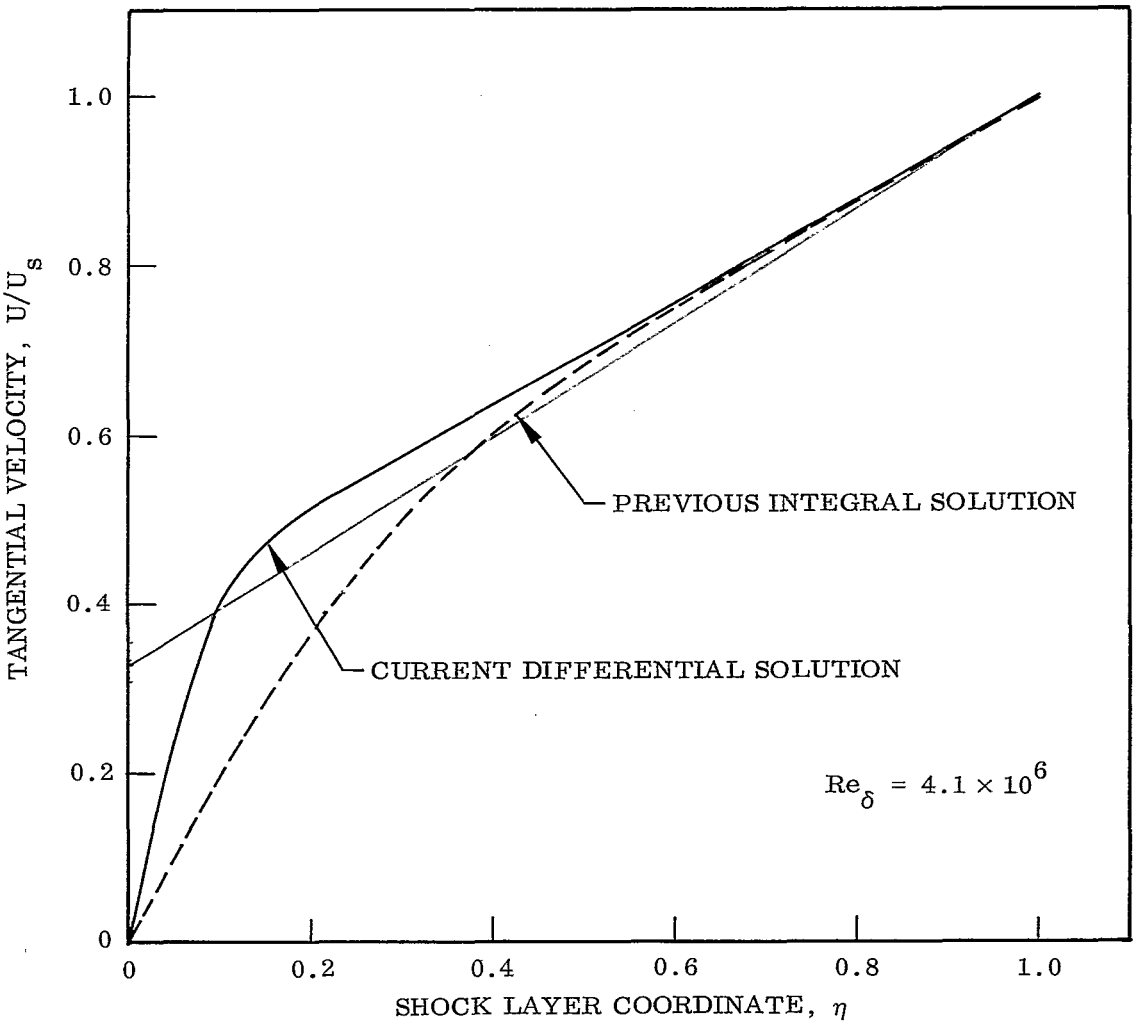

Fig. 7 Comparison of Integral Method and Differential Equation Momentum Solutions (No Mass Injection)

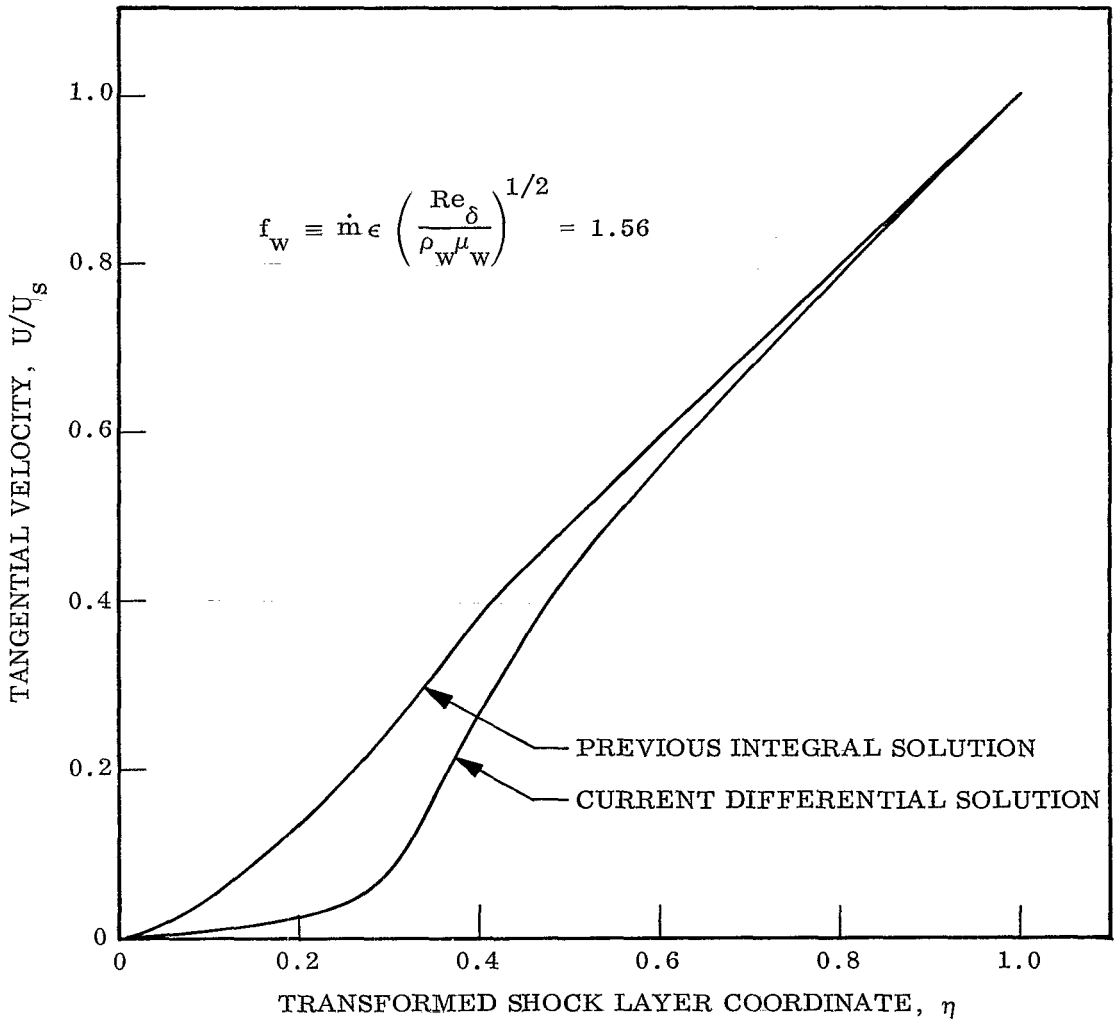

Fig. 8 Comparison of Integral Method and Differential Equation Momentum Solutions (Large Mass Injection)

calculated monochromatically at 86 frequency points and the line transport is calculated for a total of 289 "line" transitions for H, C, N, and O atoms treated in 21 "groups." From the results of a coupled flow field solution with mass injection (see the case discussed under Section 5.2), we obtain the radiative flux distributions shown in Fig. 9. Using this same case to define pressure, enthalpy and elemental composition distributions, we obtain from the RATRAP code the radiative flux values shown in comparison. The agreement is remarkably good over the entire shock layer providing confidence in our approximate transport models.

Turning now to the completely-coupled radiating shock layer problem, we have compared in Fig. 10 our current solutions with the as yet unpublished work of Page.* The flight conditions for this comparison case are:

U_∞ = 16 km/sec 52.5 kft

$\rho_\infty = 4.2 \times 10^{-7}$ gm/cm^3

alt ~ 57 km 187 kft

R = 2.34 m 7.68 ft

The close agreement seen in Fig. 10 indicates the degree of consistency which can be obtained between various investigators when all important radiating processes are included in a reasonably accurate transport model. The current level of consistency in hyperbolic entry radiative heating predictions is demonstrated more clearly in Fig. 11. Here we have taken from Fig. 15 of Ref.

---

*The author wishes to thank Mr. William Page of the NASA Ames Research Center, Hypersonic Free Flight Branch, for generously providing these results.

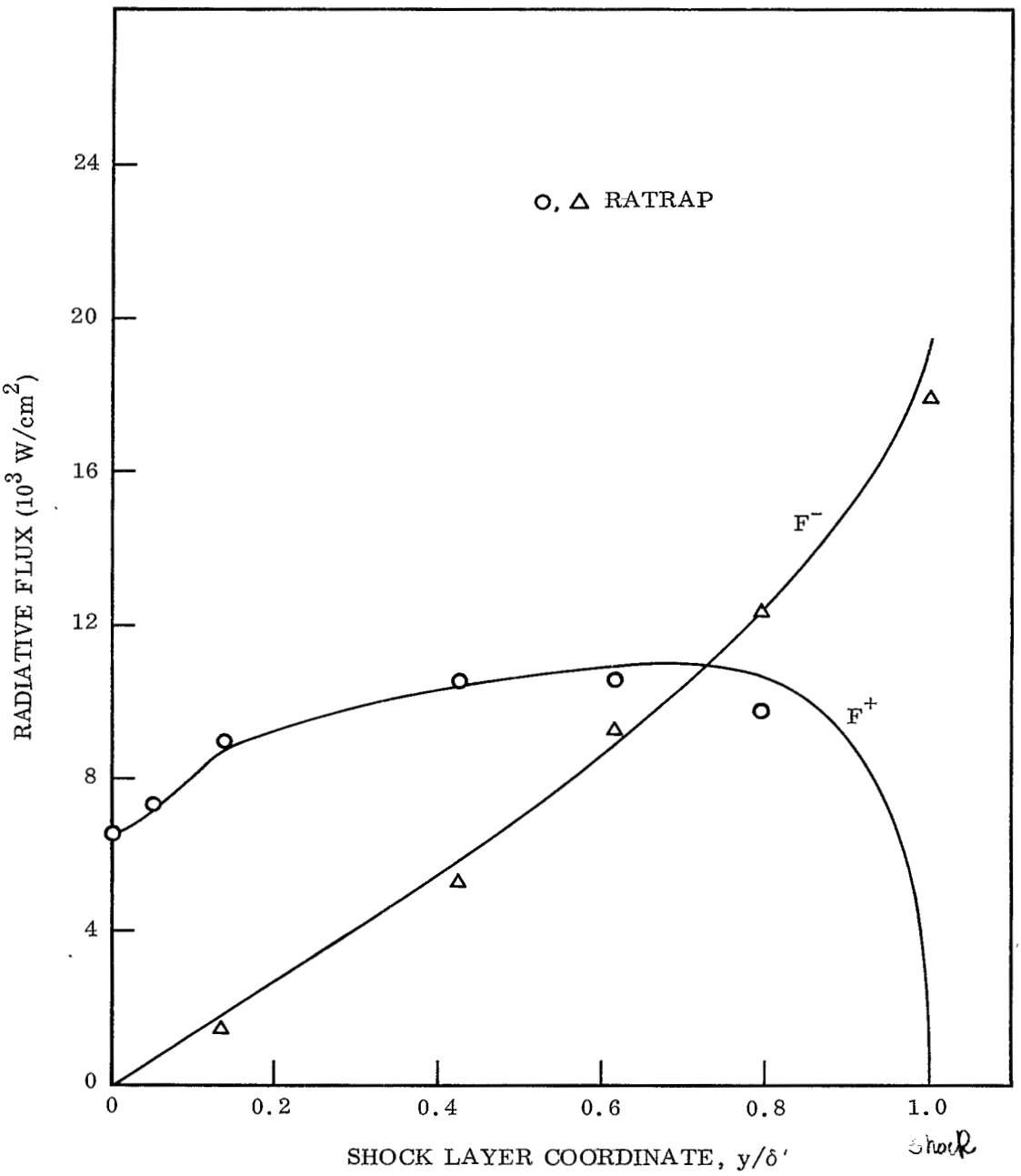

Fig. 9 Comparison of Approximate and Exact Radiative Flux Calculations

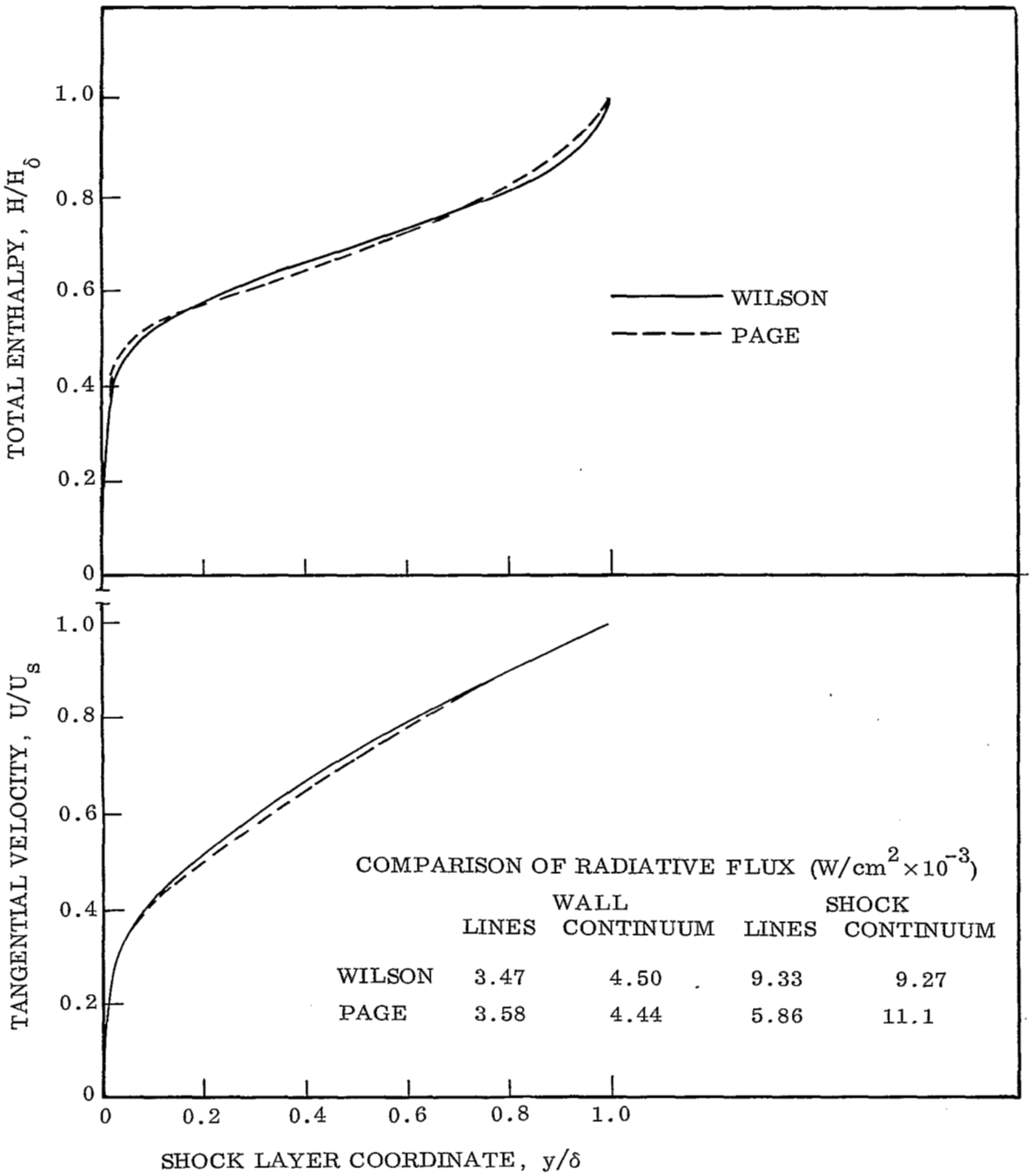

COMPARISON OF RADIATIVE FLUX ($W/cm^2 \times 10^{-3}$)

	WALL		SHOCK	
	LINES	CONTINUUM	LINES	CONTINUUM
WILSON	3.47	4.50	9.33	9.27
PAGE	3.58	4.44	5.86	11.1

Fig. 10 Comparison of Fully Coupled Radiating Viscous Solutions

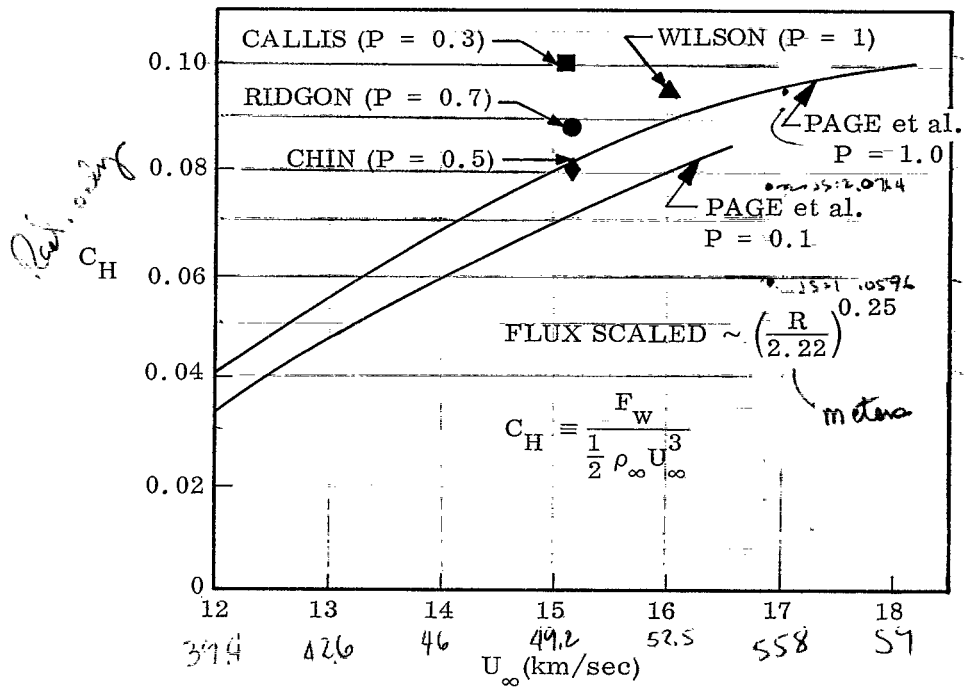

Fig. 11 Survey of Consistent Surface Radiative Flux Predictions

7, the calculations by Page et al. of the normalized surface radiative heat flux,

$$C_H \equiv \frac{F}{\frac{1}{2}\rho_\infty U_\infty^3}$$

as a function of flight velocity and for various densities yielding the two curves shown for $p = 1.0$ atm and $p = 0.1$ atm. We also have included our current results as well as those of Chin (Ref. 8), Callis (Ref. 33), and Rigdon et al. (Ref. 34). In order to account for the slightly differing body sizes in the calculations of Chin and Rigdon et al. we have scaled the radiative flux as

$$F \sim R^{.25}$$

For Chin's work, this amounts to a decrease of 6% while for the work of Rigdon et al this amounts to a decrease of 12%. It will be seen from this comparison that all five predictions lie within about 20%. We emphasize that all of these calculations account for both continuous and discrete absorption processes derived from nearly the same basic data.

5.2 SHOCK LAYER SOLUTION FOR MASSIVE BLOWING

We conclude our results with an examination of the effects of large mass injection rates on the shock layer structure and resultant surface heat flux. The flight conditions used are again the case

$U_\infty = 16$ km/sec

$\rho_\infty = 4.2 \times 10^{-7}$ gm/cm^3

alt $\sim$ 57 km

$R = 2.34$ m

and for normalized mass injection rates of $\dot{m} = .05$ and $\dot{m} = .10$. These correspond to values of the blowing parameter $f_w = 0.99$ and $f_w = 1.97$. The injected gas is the sublimation products of carbon phenolic having the elemental mass fraction composition: $C_H = .019$; $C_C = .930$; $C_N = 0$; and $C_O = .051$. The gas is injected at an enthalpy level corresponding to a sublimation temperature of 3,300 ^oK.*

The tangential velocity distribution in the transformed η coordinate is shown in Fig. 12 along with the solution for $\dot{m} = 0$. The degree to which the shear layer is detached from the wall is clearly demonstrated. For the highest injection rate, we have treated the region from the wall to $\eta = .4$ as inviscid (cf. Section 2.1).

The enthalpy distribution is shown in Fig. 13. Again we observe the detachment from the wall of the region where conductive transport plays an important role. For the highest injection rate there is a virtual absence of conduction at the wall and the convective heating is reduced by four orders of magnitude. We have replotted these enthalpy distributions in the physical coordinate y/δ in Fig. 14. Because of the high density of the low temperature ablation gases, the physical extent of the ablation layer is small. This reflects the fact that, due to the high density, the velocity and hence momentum of the ablation gases is much less than that of the incoming air stream (the momentum ratio at the wall is $M_w/M_\infty = 4 \times 10^{-5}$) and hence unable to penetrate far from the wall.

---

*Note that due to the energy of formation of certain molecular species, the absolute enthalpy of the ablation product is negative at this temperature (cf. Table I, Section 4.1).

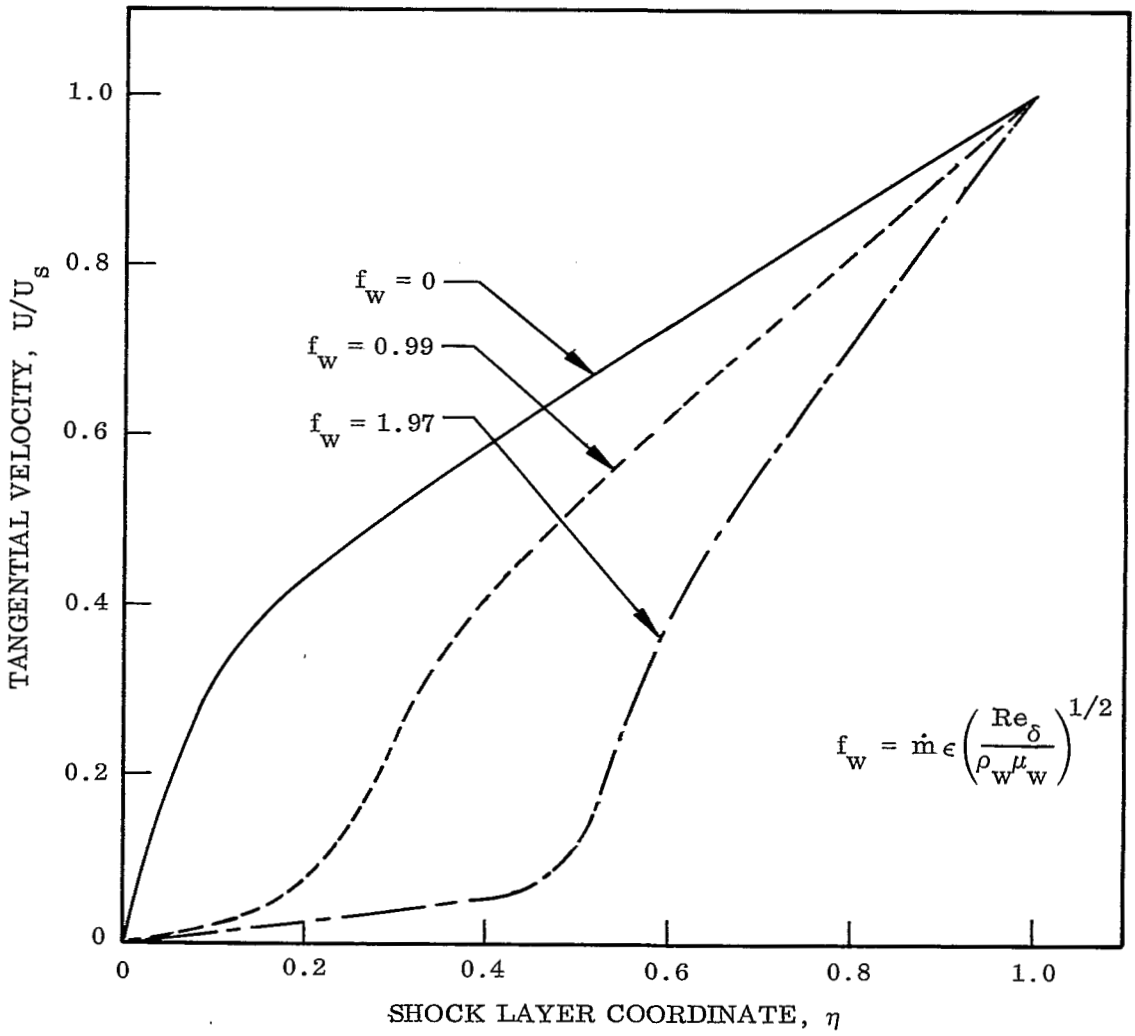

Fig. 12 Tangential Velocity Solutions for Various Mass Injection Rates

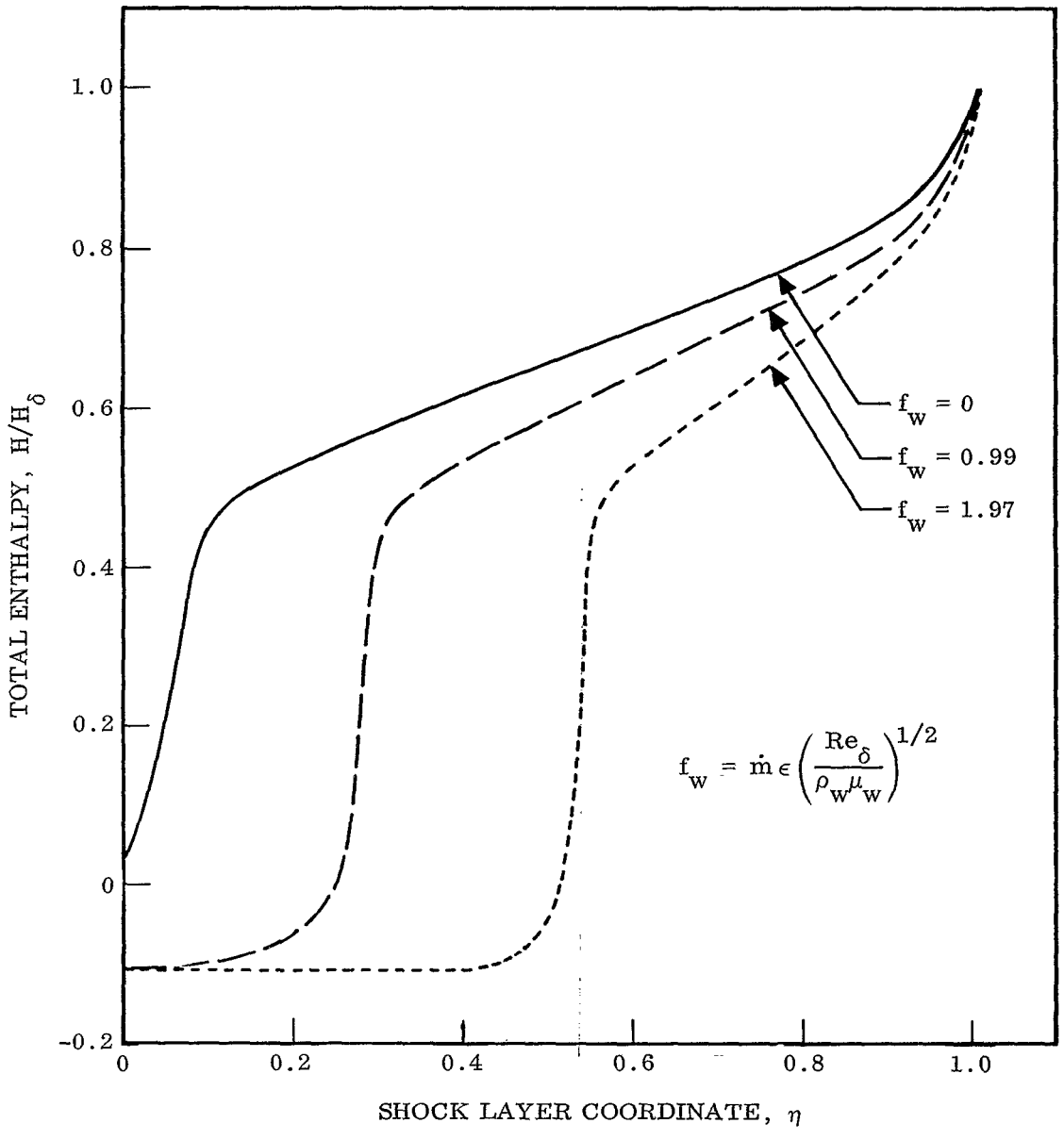

Fig. 13 Enthalpy Solutions for Various Mass Injection Rates

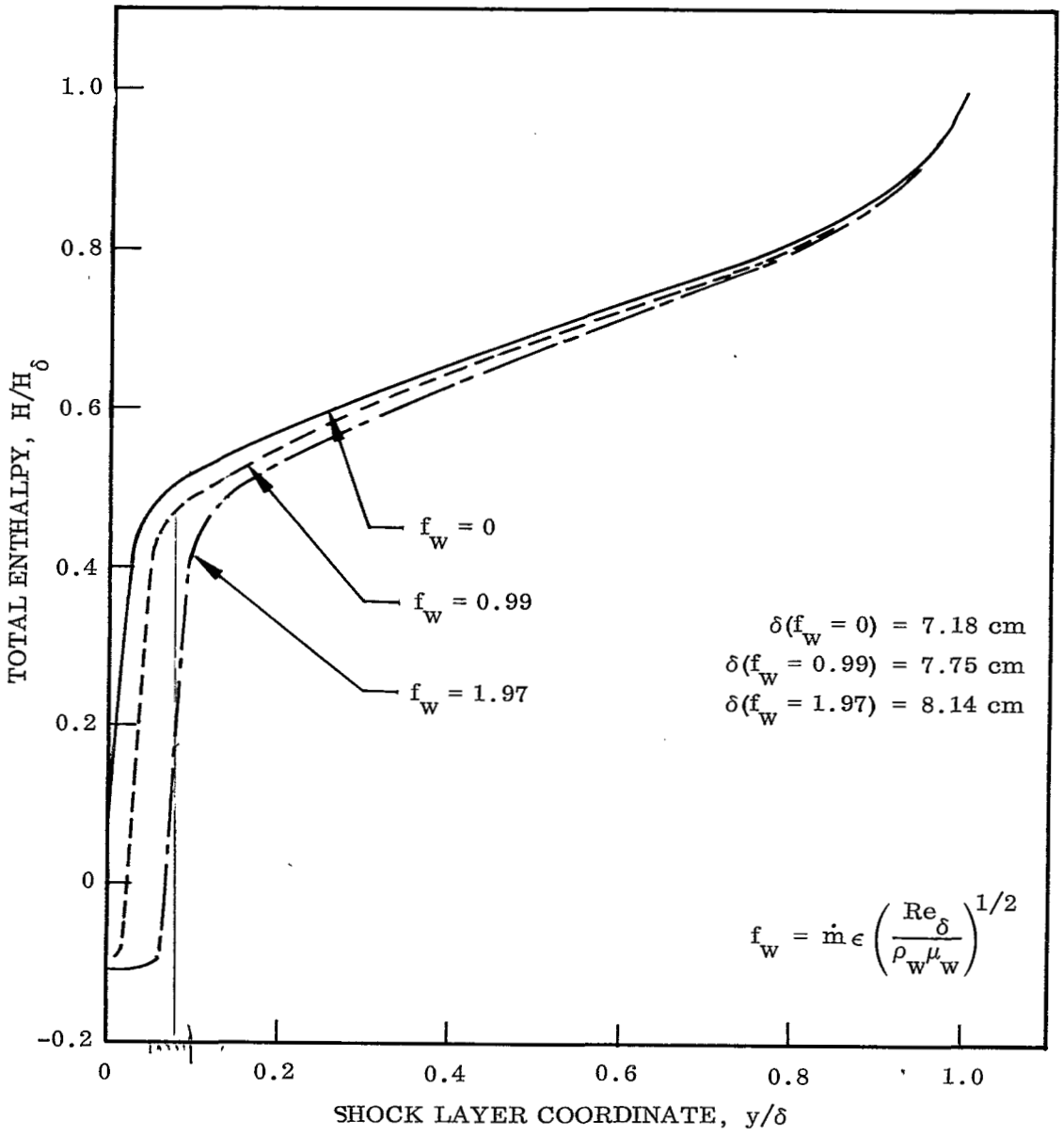

Fig. 14 Enthalpy Distributions in the Physical Coordinate for Various Mass Injection Rates

The prime objective of this study was to investigate the interaction of the ablation products with the radiant energy emitted by the high temperature air layer. As part of this question it is of interest to ask what is the role of collisional transport (i.e. "viscous" effects) in this interaction process. The distribution of the radiative flux divergence expression across the shock layer is shown in Fig. 15 for the case where $f_w = .99$. The large peak in the flux divergence is due to absorption by neutral carbon atoms (in the ground and low lying excited states) which appear in the heated ablation gases. Fig. 16 shows the spatial distribution of neutral carbon atoms and, for comparison purposes, the velocity, enthalpy, and ablation product profiles. Comparison of Figs. 15 and 16 demonstrates that the peak in the flux divergence coincides with the peak in the neutral carbon atom distribution. Moreover, as seen from Fig. 16, the large increase in neutral carbon atoms occurs in the region where viscous effects exist, as clearly indicated by the velocity and ablation product profiles. Thus it appears as though viscous effects (namely, conduction) are responsible for the rapid increase in enthalpy which in turn results in the rapid rise in carbon atoms and subsequent radiant energy absorption. However, this is not the correct interpretation.

The rate of heating of the ablation gases by absorption of radiation exceeds that due to conduction. Actually viscous effects only spread-out the region of enthalpy rise over a somewhat larger spatial extent than would be calculated in the basis of an inviscid calculation. Indeed the inviscid calculation of Ref. 8 (a calculation for a mass flux and Reynolds number condition quite similar to the case being discussed here) shows a similar rapid enthalpy rise

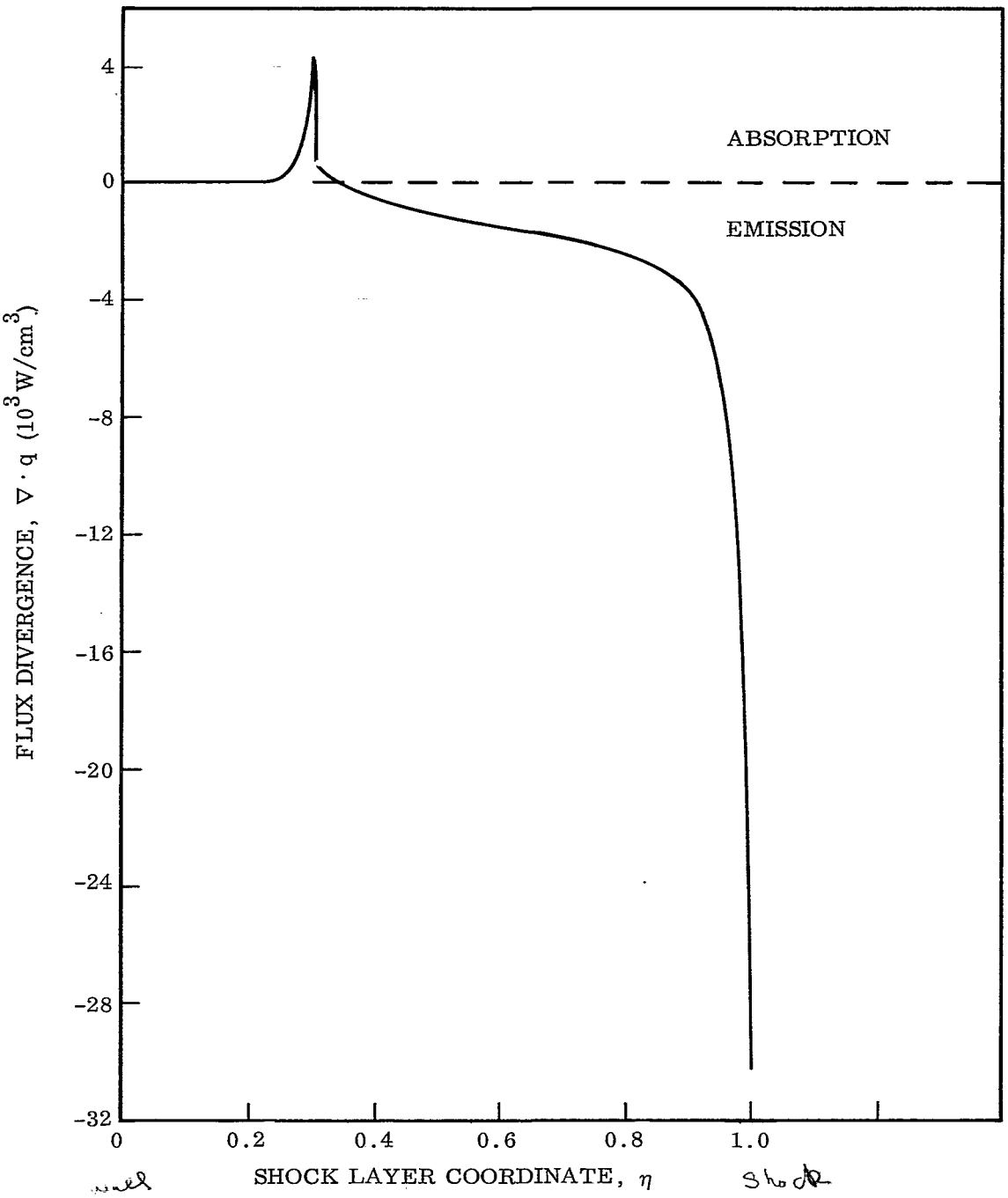

Fig. 15 Radiative Flux Divergence Distribution Across Shock Layer

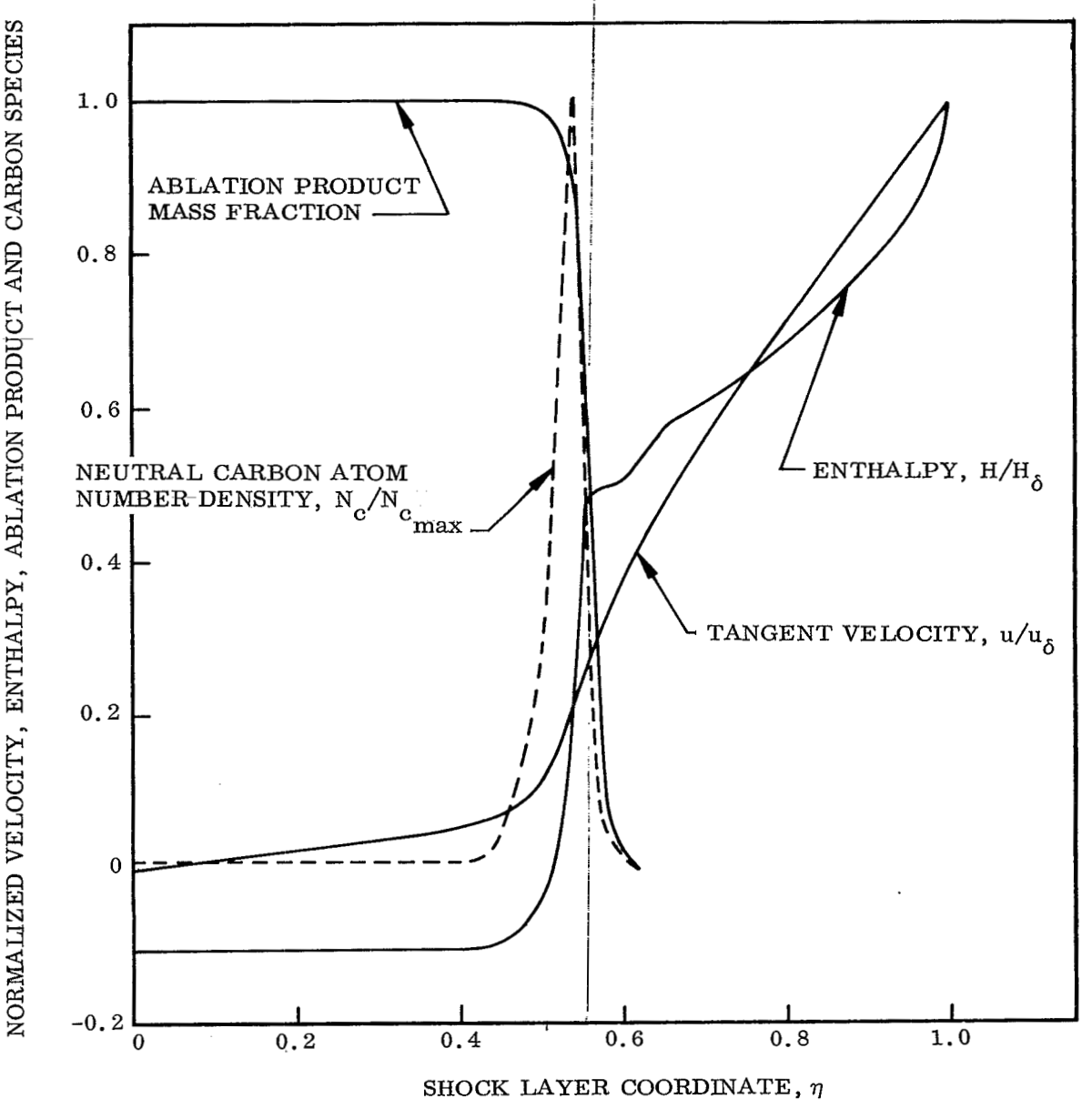

Fig. 16 Shock Layer Velocity, Enthalpy and Number Density Distributions For The Maximum Blowing Condition

also. Thus, while viscous effects influences the species and velocity distributions somewhat (the inviscid calculations tend to predict a lower tangential velocity in the ablation product gases and a correspondingly larger ablation product layer), viscous effects are of minor importance in the coupled process of heating and absorption of the ablation product gases.

The spectral nature of the ablation product absorption processes are seen more clearly by examining Fig. 17. Here we plot the spectral radiative flux at the wall for the coninuum and line contributions, in terms of the average spectral value for each continuum band and line group.* We compare the spectral distribution of the surface flux with and without mass injection. Note the significant decrease in the vacuum ultraviolet continuum emission with mass injection. This blocking effect by neutral carbon atoms due to the spectral location of its photoionization edges was reported in Refs. 9 and 10. However, the heated carbon atoms emit both continuum and line radiation. When the line emission by carbon atoms is properly calculated, it is found that the carbon atoms emit about as much as they absorb. Note the increased emission in line groups 1, 2, 3, 4. That is, for the flight condition examined, mass injection has little net effect on the surface radiative line flux. Hence the efficiency of a carbon-hydrogen mixture injected gas in shielding the surface from emission by the high temperature air region is only one-half the values previously reported in Ref. 9 which considered the continuum contribution only. A comparison of the degree of surface flux reduction due to mass injection considering both continuum and line processes with the values obtained considering

* The negative values for the line flux in some groups indicate that the continuum flux is attenuated by line absorption.

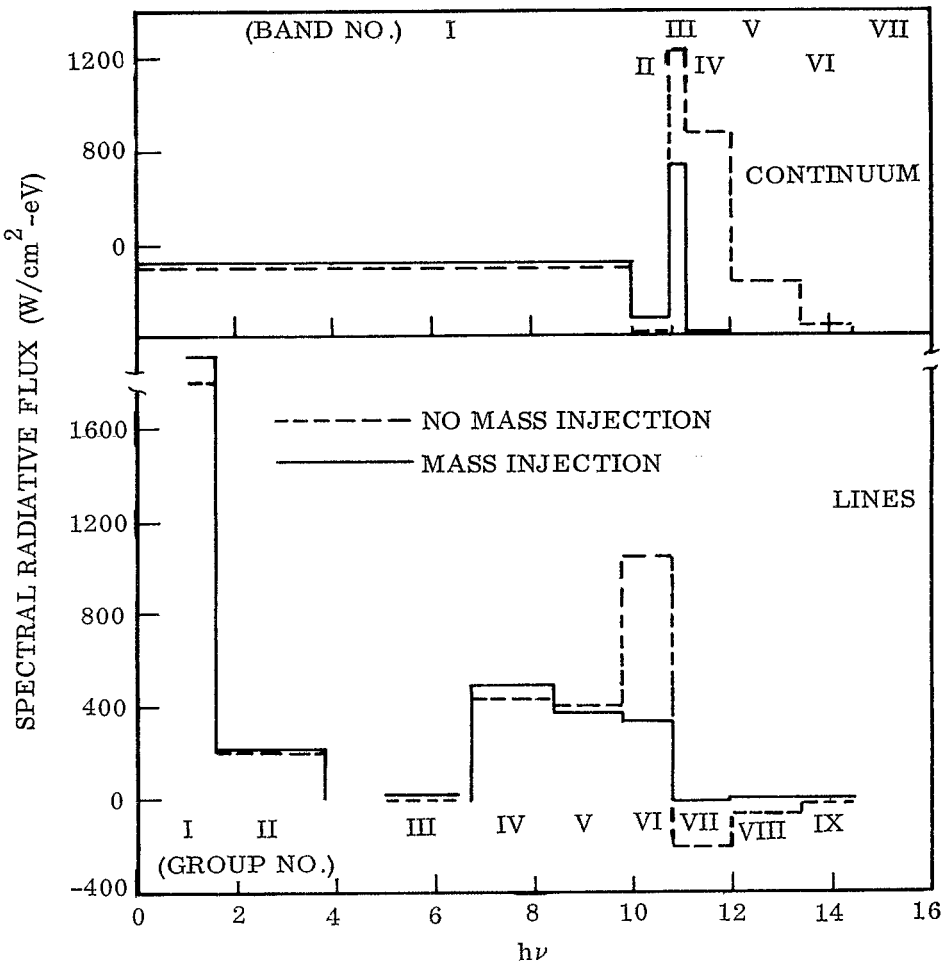

Fig. 17 Spectral Distribution of Surface Radiative Flux With and Without Mass Injection

processes only is shown in Fig. 18a. In this comparison, no molecular band absorption is included in either calculation.

In our previous studies of Ref. 9, calculations of the shock layer enthalpy distribution were made both with and without molecular band absorption included. The resulting differences in the enthalpy profile were small. Those results are further substantiated by estimates of the amount of additional ablation product heating which would occur due to molecular band absorption using the calculated spectral flux which is transmitted by the heated ablation product gases. It is found that the additional heating rates would not be adequate to increase the enthalpy levels significantly. Accordingly, an esimate of the amount of absorption due to molecular bands was made using the enthalpy profiles obtained without including molecular band absorption in the shock layer calculation. This estimate employed an uncoupled radiative transport calculation (i.e. RATRAP code) and are given in Fig. 18b. Also shown on Fig. 18b are the results of Chin's calculation (Ref. 8) in which he considers continuum processes (including molecular bands) but nitrogen lines only. We observe that Chin's value lies close to the older continuum-only flux reduction level. This is further evidence that carbon lines should be included and due to emission from these lines, a smaller degree of flux reduction results. Finally, Fig. 19 compares the spectral flux distribution of the surface with and without molecular band absorption as obtained from the uncoupled RATRAP calculation. The location of the spectral regions of increased absorption identified the following molecular band systems important in absorption: CO 4th positive; C_2 Mulliken, Freymark, and Fox-Herzberg.

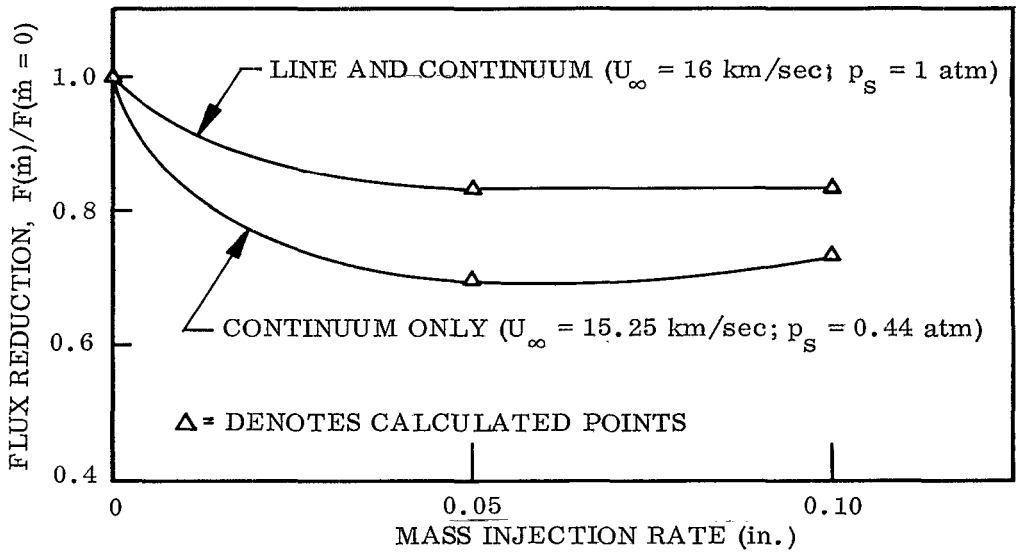

(a) Molecular Band Absorption Omitted

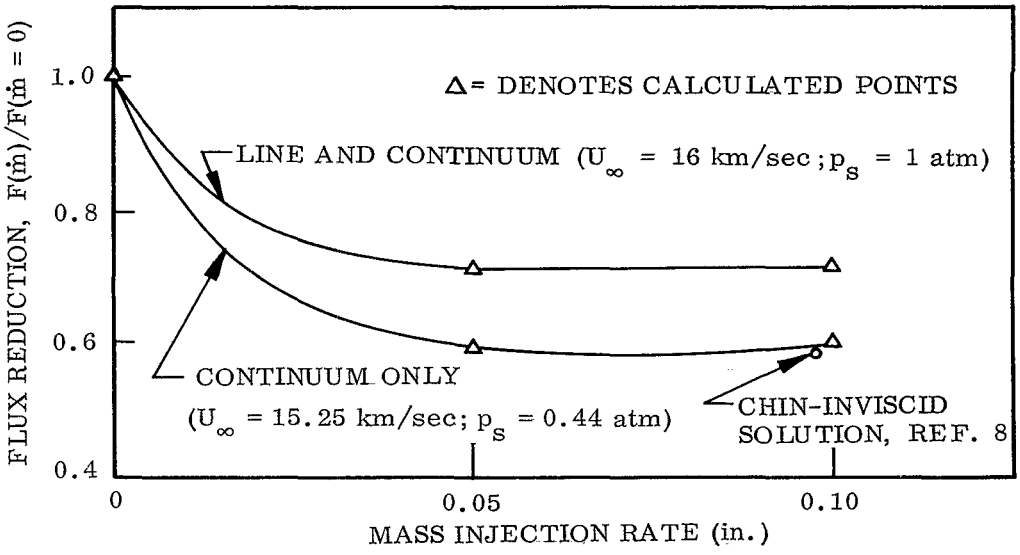

(b) Molecular Band Absorption Included

Fig. 18 The Effect of Mass Injection on Surface Flux Reduction

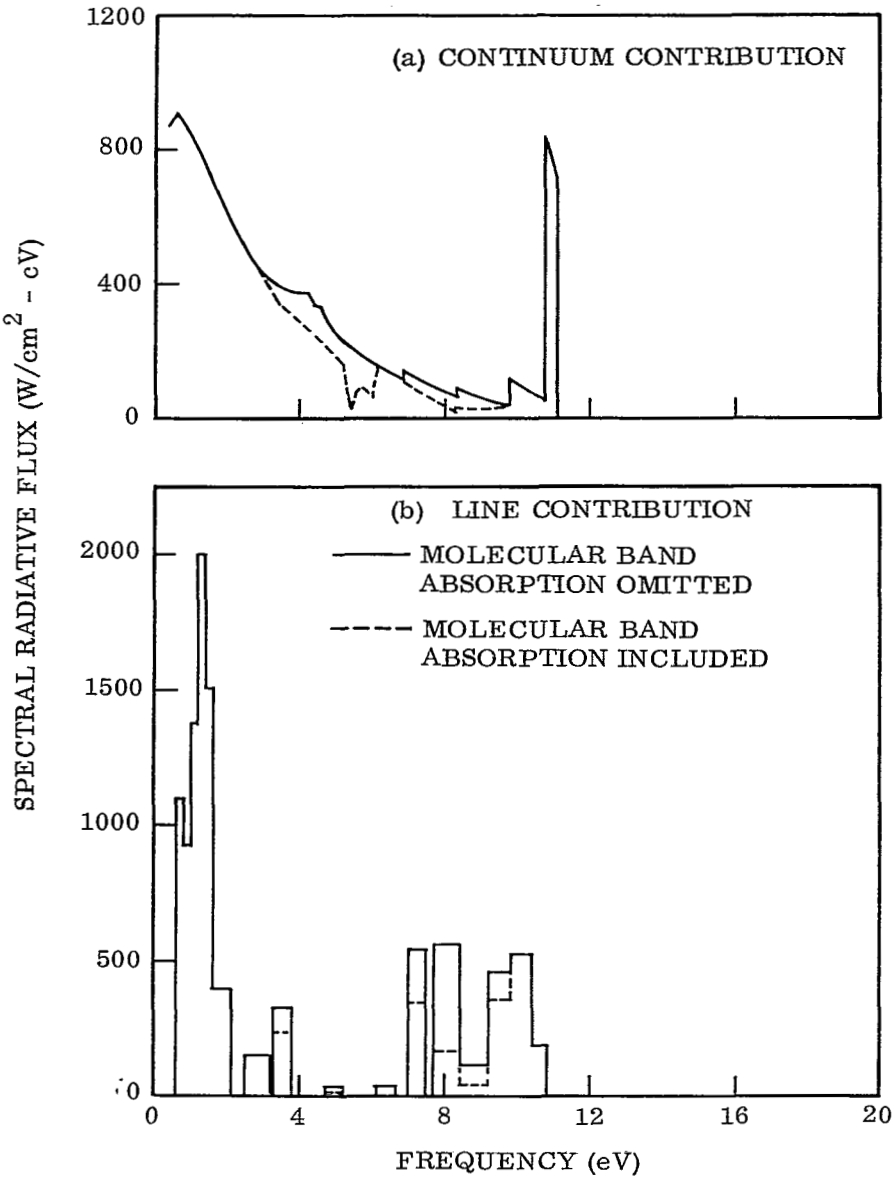

Fig. 19 Effect of Molecular Band Absorption on Surface Radiative Flux Spectral Distribution

Section 6
CONCLUDING REMARKS

The current effort has resulted in the following developments:

- The previous integral-method velocity field solution was inadequate for the large mass injection and/or Reynolds number flows of interest.
- The current computational method for solving the differential momentum equation is straightforward, numerically stable, and applies to large mass injection problems.
- The line transport model was revised to provide a consistent treatment of the nonhomogeneous transport problem for arbitrary mixtures of carbon, hydrogen, oxygen, and nitrogen atoms.
- A comparison with the work of other investigators shows that, when both line and continuum processes are accounted for, radiative heating rates at hyperbolic entry velocities are in good agreement for the no-blowing case.
- The proper accounting of line transport, particularly of carbon lines, results in the fact that the radiation flux reduction due to mass injection of carbon-hydrogen mixture is only about one-half the level calculated from a continuum only basis.
- The role of ablation product molecular absorption becomes more significant in light of the revised line transport calculations.

Section 7
REFERENCES

1. Howe, J. T. and Viegas, J. R., "Solutions of the Ionized Radiating Shock Layer, Including Reabsorption and Foreign Species Effects, and Stagnation Region Heat Transfer," NASA TR-R-159, 1963.

2. Wilson, K. H. and Hoshizaki, H., "Inviscid, Nonadiabatic Flow About Blunt Bodies," AIAA J., 3, 67-74, 1965.

3. Hoshizaki, H. and Wilson, K. H., "The Viscous, Radiating Shock Layer About a Blunt Body," AIAA J., 3, 1614-1622, 1965.

4. Hoshizaki, H. and Wilson, K. H., "Convective and Radiative Heat Transfer During Superorbital Entry," AIAA J., 5, 25-35, 1967.

5. Biberman, L. M. et al., "Radiation Heating in Hypersonic Flow," Cosmic Research 2, 376-387, 1964.

6. Dirling, R. B., Jr., Rigdon, W. S. and Thomas, M., "Stagnation-Point Heating Including Spectral Radiative Transfer," Proceedings of 1967 Heat Transfer and Fluid Mechanics Institute, June 1967.

7. Page, W. A., Compton, D. L., Borucki, W. J., Ciffone, D. L. and Cooper, D. M., "Radiation Transport in Inviscid Nonadiabatic Stagnation-Region Shock Layers," AIAA Paper No. 68-784, AIAA 3rd Thermophysics Conference, June 1968.

8. Chin, J. H., "Radiation Transport for Stagnation Flows Including the Effects of Lines and Ablation Layer," AIAA Paper No. 68-664, AIAA Fluid and Plasma Dynamics Meeting, June 1968.

9. Wilson, K. H. and Hoshizaki, H., "Effect of Ablation Product Absorption and Line Transitions on Shock Layer Radiative Transport," NASA CR-1264, February 1969.

10. Hoshizaki, H. and Lasher, L. E., "Convective and Radiative Heat Transfer to an Ablating Body," AIAA J., 6, 1441-1449, 1968.

11. Ho, H. T. and Probstein, R. F., "The Compressible Viscous Shock Layer in Rarefied Hypersonic Flow," in Rarefied Gas Dynamics, Ed. L. Tablot, Academic Press, N. Y., 1961.

12. Lees, L., "Convective Heat Transfer with Mass Addition and Chemical Reactions," Combustion and Propulsion, Third AGARD Colloquium, 1958.

13. Kendall, R. M. and Bartlett, E. P., "Nonsimilar Solution of the Multicomponent Laminar Boundary Layer by an Integral-Matrix Method," AIAA J., 6, 1089-1097, 1968.

14. Hoshizaki, H. and Lasher, L. E., "Convective and Radiative Heat Transfer to an Ablating Body," LMSC 4-06-66-12, July 1966.

15. Allen R. A., "Radiation Graphs, Spectrally Integrated Fluxes Including Line Contributions and Self-Absorption," AVCO-Everett Research Laboratory, RR-230, September 1965.

16. Zel'dovich, Ya. B. and Raizer, Yu. P., Physics of Shock Waves and High-Temperature Hydrodynamic Phenomena, Chap. II, Academic Press, New York, 1966.

17. Wilson, K. H. and Greif, R., "Radiation Transport in Atomic Plasmas," JQSRT, 8, 1061-1086, 1968.

18. Wilson, K. H. and Nicolet, W. E., "Spectral Absorption Coefficients of Carbon, Nitrogen and Oxygen Atoms," JQSRT, 7, 891-941, 1967.

19. Goody, R. M., Atmospheric Radiation, Oxford University Press, New York, 1964.

20. Wilson, K. H. and R. Greif, "Atomic Line Transport in Nonhomogeneous Gases," to be issued as LMSC report.

21. Plass, G. N., "Equivalent Width Due to Two Overlapping Lines," J. Opt. Soc. Am., 55, 104, 1965.

22. Browne, H. N., Williams, M. W. and Cruise, D. R., "The Theoretical Computation of Equilibrium Compositions, Thermodynamic Properties and Perform ance Characteristics of Propellant Systems," NAWEPS Report 7043, June 1968.

23. Steinbach, G. R., "Users Manual for the Free Energy Minimization Program," LMSC TXN-2502 (Interdepartmental Memorandum), August 1967.

24. Buddenburg, J. W. and Wilke, C. R., Ind. Eng. Chem., 41, 1345, 1949.

25. Mason, E. A. and Saxena, S. C., "Approximate Formula for the Thermal Conductivity of Gas Mixtures," Physics of Fluids, 1, 361-369, 1968.

26. Blake, L. H., "Approximate Transport Calculations for High Temperature Air," LMSC 6-78-69-20, May 1969.

27. Hirschfelder, J. O., Curtiss, C. F. and Bird, R. B., Molecular Theory of Gases and Liquids, J. Wiley & Sons, Inc., New York, 1954.

28. Kennard, E. H., Kinetic Theory of Gases, McGraw-Hill Book Co., Inc., New York, 1938.

29. DeRienzo, P. and Pallone, A., "Convective Stagnation Point Heating for Reentry Speeds up to 70,000 ft/sec Including Effects of Large Blowing Rates," AVCO R&D Div., RAD-TM-65-58, January 1966.

30. Yun, K. S., Weissman, S. and Mason, E. A., "High Temperature Transport Properties of Dissociating Nitrogen and Dissociating Oxygen," Physics of Fluids, 5, 672-678, 1962.

31. Predvoditelev, A. S., Charts of the Thermodynamic Functions of Air, Translated by Associated Technical Services, Inc., Glen Ridge, New Jersey, 1962.

32. Hansen, C. F., "Approximations for the Thermodynamic and Transport Properties of High-Temperature Air," NASA TR-R-50, 1959.

33. Callis, L. B., "Time Asymptotic Solutions of Blunt-Body Stagnation-Region Flows with Nongray Emission and Absorption of Radiation," AIAA Paper No. 68-663, AIAA Fluid and Plasma Dynamics Conference, 1968.

34. Rigdon, W. S., Dirling, R. B., Jr. and Thomas, M., "Radiative and Convective Heating During Atmospheric Entry," Douglas Aircraft Co., Missile & Space Div., DAC-60913, March 1968.

35. Lasher, L. E., Wilson, K. H. and Greif, R., "Radiation From an Isothermal Hydrogen Plasma at Temperatures up to 40,000 ^{o}K," LMSC 6-76-66-17 (Revised), July 1967.

36. Griem, H. R., Plasma Spectroscopy, McGraw-Hill Book Co., Inc., New York, 1964.

Appendix A

EQUATIONS FOR AVERAGED CONTINUUM ABSORPTION COEFFICIENTS

The continuum transport is calculated using a 7-band model. In each group we calculate

$$\mu = N_H\sigma_H + N_C\sigma_C + N_N\sigma_N + N_O\sigma_O$$

The equations for the band-averaged absorption cross section are listed below.

Group 1: $0 \le h\nu \le 10.00$ eV

In band one we use a partial Planck mean in which σ_i for each element has the general form

$$\sigma_i = \frac{5.04\text{x}10^3\ kT\ \Gamma_i\ K_o\ e^{-\epsilon_i/kT}}{B_P} e^{\Delta/kT}\ h\nu_T^{\,i}\left[\alpha_i + \frac{\beta_i}{3}(h\nu_T^{\,i})^2\right]$$

$$+ kT\left[\alpha_i + 2\beta_i(kT)^2\right] - kT\ e^{-(h\nu_B - h\nu_T^{\,i})/kT}\left[\alpha_i + \beta_i(h\nu_B - h\nu_T^{\,i})^2\right]$$

$$- kT\ e^{-(h\nu_B - h\nu_T^{\,i})}\left[2\beta_i(h\nu_B - h\nu_T^{\,i})(kT) + 2\beta_i(kT)^2\right]$$

where $K_o = 7.26^{-16}\ \text{cm}^2\text{eV}^2$

$h\nu_B = 10.00$ eV

and

$$B_P = 5.04 \times 10^3 (kT)^4 \left\{ \frac{\pi^4}{15} - e^{-h\nu_B/kT} \left[\left(\frac{h\nu_B}{kT}\right)^3 + 3\left(\frac{h\nu_B}{kT}\right)^2 + 6\left(\frac{h\nu_B}{kT}\right) + 6 \right] \right\}$$

For each specie i we have the parameters

Hydrogen: $h\nu_T^i = 2.40$ eV $\quad \epsilon_i = 13.56$ eV

$\alpha_i = 1.00 \quad \beta_i = 0$

Carbon: $h\nu_T^i = 3.78$ eV $\quad \epsilon_i = 11.26$ eV

$\alpha_i = 0.30 \quad \beta_i = 0.0488$

Nitrogen: $h\nu_T^i = 4.22$ eV $\quad \epsilon_i = 14.54$ eV

$\alpha_i = 0.24 \quad \beta_i = 0.0426$

Oxygen: $h\nu_T^i = 4.22$ eV $\quad \epsilon_i = 13.61$ eV

$\alpha_i = 0.24 \quad \beta_i = 0.0426$

Group 2: $10.0 \text{ eV} \leq h\nu \leq 10.80 \text{ eV}$

$$\sigma_H = 0 \; ; \; \sigma_N = 0 \; ; \; \sigma_O = 0$$

$$\sigma_C = \frac{8.5^{-17} \, e^{-1.26/kT} + 2.2^{-17} \, e^{-2.75/kT} + 5.0^{-17} \, e^{-4.18/kT}}{\Sigma_C}$$

Group 3: $10.80 \text{ eV} \leq h\nu \leq 11.1 \text{ eV}$

$$\sigma_H = 0 \quad ; \quad \sigma_O = 0$$

$$\sigma_C = \frac{1}{\Sigma_C}\left[8.5^{-17}\ e^{-1.26/kT} + 2.2^{-17}\ e^{-2.75/kT} + 5.0^{-17}\ e^{-4.18/kT}\right]$$

$$\sigma_N = \frac{1}{\Sigma_N}\left[5.16^{-17}\ e^{-3.50/kT}\right]$$

Group 4: $11.1 \leq h\nu \leq 12.0$

$$\sigma_H = 0 \quad \sigma_O = 0$$

$$\sigma_C = \frac{1}{\Sigma_C}\left[9.9^{-17} + 8.5^{-17}\ e^{-1.26/kT} + 2.2^{-17}\ e^{-2.75/kT} + 5.0^{-17}\ e^{-4.18/kT}\right.$$

$$\sigma_N = \frac{1}{\Sigma_N}\left[5.16^{-17}\ e^{-3.50/kT}\right]$$

Group 5: $12.0\ eV \leq h\nu \leq 13.4\ eV$

$$\sigma_H = 0 \quad ; \quad \sigma_O = 0$$

$$\sigma_C = \frac{1}{\Sigma_C}\left[9.9^{-17} + 8.5^{-17}\ e^{-1.26/kT} + 2.2^{-17}\ e^{-2.75/kT} + 5.0^{-17}\ e^{-4.18/kT}\right]$$

$$\sigma_N = \frac{1}{\Sigma_N}\left[6.4^{-17}\ e^{-2.30/kT} + 5.16^{-17}\ e^{-3.50/kT}\right]$$

Group 6: $13.4\ eV \leq h\nu \leq 14.3\ eV$

$$\sigma_H = \frac{1.18^{-17}}{\Sigma_H}$$

$$\sigma_C = \frac{1}{\Sigma_C}\left[9.9^{-17} + 8.5^{-17}\ e^{-1.26/kT} + 2.2^{-17} e^{-2.75/kT} + 5.0^{-17} e^{-4.18/kT}\right]$$

$$\sigma_O = \frac{3.6^{-17}}{\Sigma_O}$$

$$\sigma_N = \frac{1}{\Sigma_N}\left[6.4^{-17}\ e^{-2.30/kT} + 5.16^{-17}\ e^{-3.50/kT}\right]$$

Group 7: $14.3\ \text{eV} \leq h\nu \leq 20.0\ \text{eV}$

$$\sigma_H = \frac{1.18^{-17}}{\Sigma_H} \quad ; \quad \sigma_O = \frac{3.6^{-17}}{\Sigma_O}$$

$$\sigma_C = \frac{1}{\Sigma_C}\left[9.9^{-17} + 8.5^{-17}\ e^{-1.26/kT} + 2.2^{-17}\ e^{-2.75/kT} + 5.0^{-17}\ e^{-4.18/kT}\right]$$

$$\sigma_N = \frac{1}{\Sigma_N}\left[3.6^{-17} + 6.4^{-17}\ e^{-2.30/kT} + 5.16^{-17}\ e^{-3.50/kT}\right]$$

Appendix B

EFFECTIVE LINE PARAMETERS

We derived in Section 3.4 the following expressions for the effective f-number and half-width for transitions in atom i,

$$f_i^* = \frac{1}{n_i} \sum_m \frac{f_m g_m e^{-\epsilon_m/kT}}{\Sigma_i}$$

$$\beta_i^* = \frac{1}{n_i^2 f_i^*} \sum_m \left[\frac{f_m \beta_m g_m e^{-\epsilon_m/kT}}{\Sigma_i} \right]^{1/2}$$

Collecting all transitions which arise from a common lower state ℓ we can rewrite these expressions as

$$f_i^* = \frac{1}{n^i} \sum_\ell f_\ell^i \, P_\ell^i$$

$$\beta_i^* = \frac{1}{n_i^2 f_i^*} \sum_\ell (f\beta_\ell^i)^{1/2} (P_\ell^i)^{1/2}$$

where P_ℓ^i is the fractional population of state ℓ in specie i,

$$P_\ell^i = \frac{g_\ell e^{-\epsilon_\ell/kT}}{\Sigma_i}$$

and

$$f_\ell^{\,i} = \sum_{m \text{ in } \ell} f_m$$

$$(f\beta_\ell^{\,i})^{1/2} = \sum_{m \text{ in } \ell} (f_m \beta_m)^{1/2}$$

The states ℓ considered for H, C, N and O are listed in Table B-1.

The spectral composition of the lines is shown by the data given in Table B-2. In this table we list the nine line groups used in calculating the total line transport. For each line group we list its spectral location and its spectral interval. For each element we list the number of lines n_i in the group, and for each state ℓ of that element the parameters $f_\ell^{\,i}$ and $(f\beta_\ell^{\,i})^{1/2}$. These line parameters were obtained using the tabulated f-numbers and half-widths from Wilson and Nicolet (Ref. 18) for C, N and O atoms. For H atoms, the investigation of Lasher, Wilson, and Greif (Ref. 35) showed that almost all the line transport is accounted for by the first three members of the Lyman and Balmer series. Hence only these six lines were included. The f-numbers were taken from Griem (Ref. 36) and the half-widths determined by matching a Lorentzian profile to the asymptotic wing shape of Griem.

TABLE B-1

FRACTIONAL POPULATION DATA

Element i	State ℓ	g_ℓ	ϵ_ℓ
H	1	2	0
	2	8	10.20
C	1	9	0
	2	5	1.264
	3	1	2.684
	4	5	4.183
	5	12	7.532
	6	36	8.722
	7	60	9.724
N	1	4	0
	2	10	2.384
	3	6	3.576
	4	18	10.452
	5	54	11.877
	6	90	13.002
O	1	9	0
	2	5	1.967
	3	1	3.188
	4	8	9.283
	5	24	10.830
	6	40	12.077

TABLE B-2

LINE GROUP DATA

Group No. j	Center Frequency $h\nu^j$	Spectral Interval D^j	Element i	Number of lines n_i	State ℓ	f^i_ℓ	$(f\beta^i_\ell)^{1/2}$
1	1.30 eV	.600 eV	C	28	5	1.16	7.42^{-11}
					6	1.12	1.91^{-10}
					7	9.97^{-1}	4.89^{-9}
			N	30	4	2.08^{-1}	1.48^{-11}
					5	1.52	2.26^{-10}
					6	1.12	4.79^{-10}
			O	10	5	1.04	1.22^{-10}
					6	1.14	2.87^{-10}
2	2.70 eV	2.20 eV	H	3	2	8.05^{-1}	2.37^{-10}
			C	7	5	4.06^{-2}	9.40^{-12}
					6	6.98^{-2}	7.94^{-11}
			N	16	4	9.08^{-1}	1.64^{-10}
					5	3.15^{-2}	7.01^{-11}
			O	11	4	1.02	6.13^{-11}
					5	8.25^{-2}	7.19^{-11}
3	5.75 eV	1.50 eV	C	2	2	7.29^{-2}	9.18^{-12}
					3	6.76^{-2}	8.75^{-12}
4	7.57 eV	1.65 eV	C	8	1	1.05^{-1}	9.57^{-12}
					2	1.10^{-2}	4.86^{-12}
					3	1.50^{-1}	5.93^{-10}
			N	2	2	7.40^{-2}	8.22^{-12}
					3	6.34^{-2}	7.60^{-12}
5	9.10 eV	1.40 eV	C	14	1	3.29^{-1}	3.65^{-11}
					2	1.18^{-1}	5.77^{-10}
					4	2.36^{-1}	6.56^{-11}
			N	4	3	1.08^{-1}	3.09^{-11}
			O	1	1	4.71^{-2}	5.08^{-12}

TABLE B-2
(Cont'd)

Group No. j	Center Frequency $h\nu^j$	Spectral Interval D^j	Element i	Number of lines n_i	State ℓ	f^i_ℓ	$(f\beta^i_\ell)^{1/2}$
6	10.40 eV	1.00 eV	H	1	1	4.16^{-1}	3.02^{-11}
			C	4	1	8.65^{-2}	2.35^{-10}
			N	16	1	1.84^{-1}	1.07^{-11}
					2	2.90^{-1}	4.41^{-11}
					3	8.64^{-2}	2.28^{-10}
			O	2	3	1.51^{-1}	9.93^{-12}
					2	1.20^{-1}	8.85^{-12}
7	11.40 eV	1.20 eV	C	6	1	4.51^{-2}	6.07^{-10}
					2	7.05^{-1}	2.10^{-10}
			N	14	1	4.54^{-1}	2.71^{-12}
					2	9.63^{-2}	2.34^{-10}
					3	1.78^{-1}	2.46^{-11}
			O	3	3	4.23^{-2}	2.52^{-11}
8	12.70 eV	1.40 eV	H	2	1	1.08^{-1}	1.32^{-10}
			C	2	1	3.79^{-1}	1.95^{-11}
					3	1.05	1.27^{-11}
			N	11	1	1.55^{-1}	2.98^{-11}
					2	1.42^{-1}	7.08^{-11}
					3	3.75^{-2}	1.33^{-10}
			O	15	1	1.46^{-1}	1.97^{-10}
					2	8.61^{-2}	1.80^{-11}
					3	9.33^{-2}	8.13^{-11}
9	13.90 eV	1.00 eV	C	1	2	2.95^{-1}	5.85^{-12}
			N	11	1	2.24^{-1}	3.41^{-10}
					2	2.92^{-2}	1.48^{-10}
			O	10	1	5.24^{-2}	5.76^{-12}
					2	7.22^{-2}	7.20^{-11}
					3	6.04^{-2}	8.05^{-11}

Appendix C
MULTICOMPONENT DIFFUSION MODEL

The diffusional processes of the multicomponent gas systems evaluated are assumed in this investigation to be of an effective binary model. That is, all species in the multicomponent gas system are assumed to diffuse as two separate gases. This model, as originally proposed by Lees (Ref. 12), is a valid description of the diffusion processes in a gas mixture if the gas consists of two groups of species, each with about the same atomic or molecular weight and about the same mutual collision cross-sections. For dissociated and partially dissociated air systems, this binary assumption has proven a valid model (Ref. 12). For the H, C, N, O, system of the mass injection system, the binary diffusion model leads to results which are not physically correct.

Because of the large difference in molecular weight of hydrogen from the other elements involved, fundamental diffusion theory would indicate that hydrogen should diffuse further away from the body surface than occurs with the binary model. It is of interest to determine the effect of a more realistic hydrogen concentration distribution upon the radiation transport within the shock layer and subsequently upon the total wall heat flux.

A description of the transport properties based on a rigorous kinetic theory substantially complicates an already difficult gasdynamic and radiation transport problem. For this reason, a simplified diffusion model was desired which

demonstrated the basic multicomponent transport characteristics without adding a prohibitive degree of additional numerical calculations. The approximate multicomponent model recently developed by Kendall and Bartlett (Ref. 13) is well suited for our purposes.

The key to the Kendall diffusion model is the approximation of the binary diffusion coefficients between the respective species considered by a correlation equation first suggested by Bird (Ref. 13). The diffusion coefficient utilized is of the form

$$D_{ij} = \frac{\bar{D}}{F_i F_j} \qquad \text{(C-1)}$$

where $\bar{D}$ is a reference diffusion coefficient and F_i might be termed a diffusion factor for species i. Equation (C-1) is really a correlation equation in that once a reference coefficient $\bar{D}$ is determined, the F_i's are determined by a least-squares fit of the D_{ij} data available for all diffusing pairs in the chemical system of interest. The definition of $\bar{D}$ is such that the F_i's are independent of temperature and pressure and therefore also independent of concentration. Hence the F_i's can be determined a priori for a given set of chemical species. The accuracies which have been obtained using this procedure are surprisingly good (Ref. 13).

The decided advantage of the correlation given by Eq. (C-1) is that the Stefan-Maxwell relation for the diffusion flux and species concentrations can be cast in a form involving properties and gradients of individual species

and of the system as a whole. This greatly simplifies the previous inter-specie relationships characteristic of the multicomponent descriptions. Neglecting thermal diffusion effects, the diffusional mass flux was shown to be (Ref. 13)

$$j_i = - \rho D_{eff} \frac{\partial Z_i}{\partial y} \tag{C-2}$$

where

$$D_{eff} \equiv \frac{\bar{D} \sum_i K_i/F_i}{M \sum_i F_i K_i/M_i}$$

and

$$Z_i = \frac{K_i/F_i}{\sum_i K_i/F_i}$$

Applying the Shvab-Zeldovich transformation (multiplication by the mass of element K in molecule i, α_{Ki}, and summing over all species) to Eq. (C-2), the elemental conservation equation can be written (in terms of our body oriented, curvilinear coordinate system as

$$f\rho u \frac{\partial \tilde{K}_K}{\partial x} + r\rho v \frac{\tilde{H}\partial \tilde{K}_K}{\partial y} = \frac{\partial}{\partial y} \left(\tilde{H} r \rho D_{eff} \frac{\partial \tilde{Z}_K}{\partial y} \right) \tag{C-3}$$

The similarity of Eq. (C-3) to the binary diffusion model is apparent. Now, transforming Eq. (C-3) into the coordinate system defined by Hoshizaki (Ref. 10), we obtain,

$$\frac{\partial}{\partial \eta} \left\{ \frac{1}{F_1} \frac{\partial \tilde{Z}_k}{\partial \eta} \right\} + F_2 \frac{\partial \tilde{K}_k}{\partial \eta} = L_1 \tag{C-4}$$

As there is not an explicit relationship between $\tilde{Z}_k$ and $\tilde{K}_k$, the solution to Eq. (C-4) must be obtained in the following iterative manner. We note that

$$\frac{\partial \tilde{Z}_k}{\partial \eta} = \frac{\partial \tilde{Z}_k}{\partial \tilde{K}_k} \frac{\partial \tilde{K}_k}{\partial \eta} \tag{C-5}$$

and

$$\frac{\partial \tilde{Z}_k}{\partial \tilde{K}_k} = \frac{\partial}{\partial \tilde{K}_k} \left[C \sum_i \frac{\alpha_{ki} K_i}{F_i} \right]$$

$$= C \sum_i \frac{\alpha_{ki}}{F_i} \frac{\partial K_i}{\partial \tilde{K}_k} \tag{C-6}$$

where $C = 1/\sum_i K_i/F_i$

If we let $P(\eta) = \frac{\partial \tilde{Z}}{\partial \tilde{K}_k}/F_i$

Equation (C-4) can be written, for the stagnation case ($L_1 = 0$), as

$$\frac{\partial}{\partial \eta} \left\{ P(\eta) \frac{\partial \tilde{K}_k}{\partial \eta} \right\} + F_2(\eta) \frac{\partial \tilde{K}_k}{\partial \eta} = 0 \tag{C-7}$$

which has the solution

$$\tilde{K}_k = \int_o^\eta \frac{C_1}{P} e^{-\int_o^\eta \frac{F_2}{P} d\eta} d\eta + C_2 \tag{C- 8}$$

C_1 and C_2 are constants of integration. Equation (C-8) reduces to the elemental concentration solution obtained by Hoshizaki (Ref.10) for the binary diffusion model (i.e., $P = 1/F_1$).

For the Kendall diffusion model, the function $P(\eta)$ is an implicit function of $\tilde{K}_k$; therefore, Eq. (C-8) must be solved in the following iterative manner: (1) the elemental concentration distributions are obtained from the binary diffusion solution; (2) from the equilibrium chemical program (FEMP), the corresponding specie concentrations are obtained; (3) the gradient of species to elemental concentrations is then determined from which P can be calculated (Eq. C-6); (4) Eq. (C-8) is then used to determine the new elemental concentrations. Steps (2) through (4) are then repeated until convergence on $\tilde{K}_k$ is obtained.

NASA-Langley, 1970 —— 33